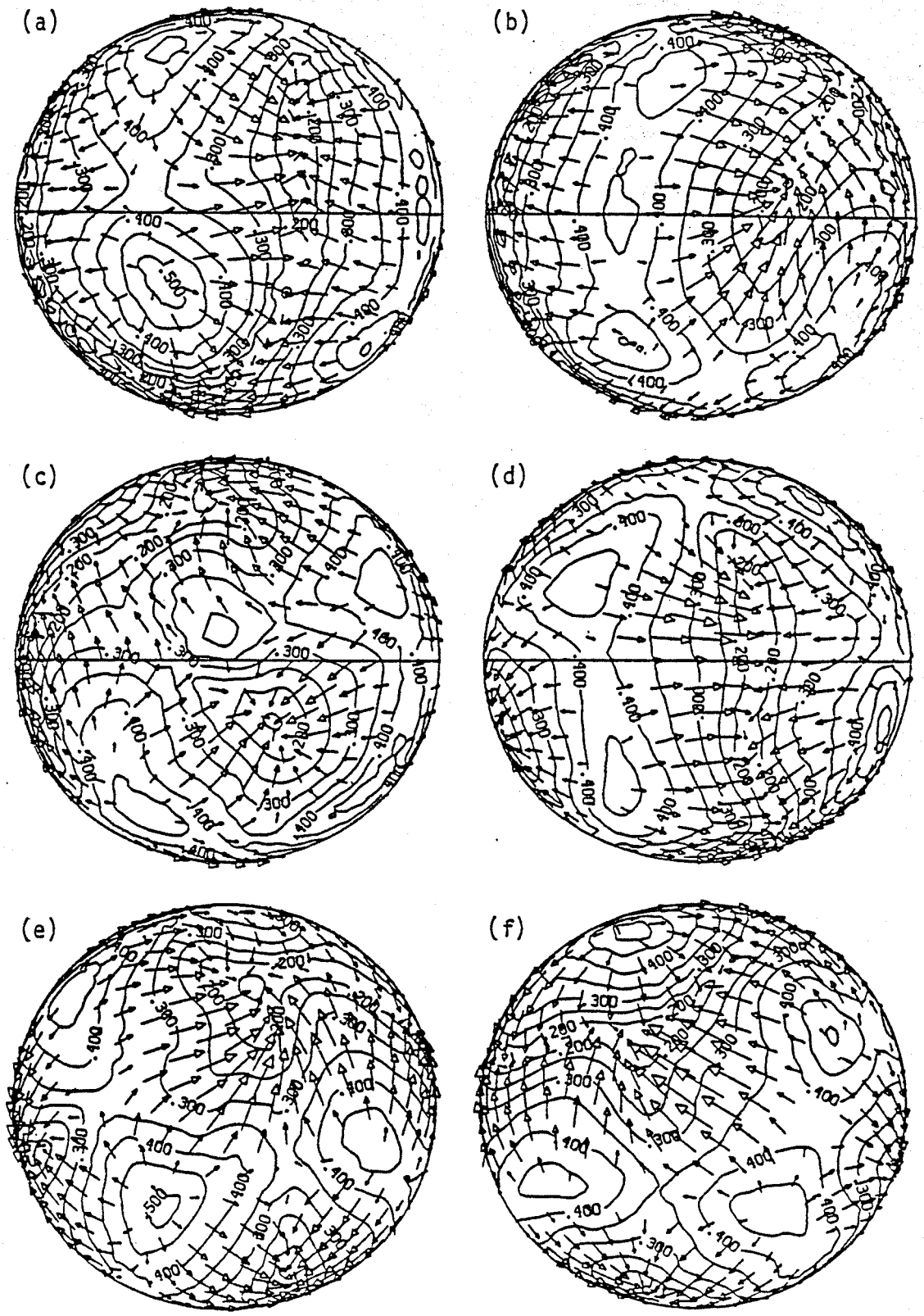

Figure 8.8

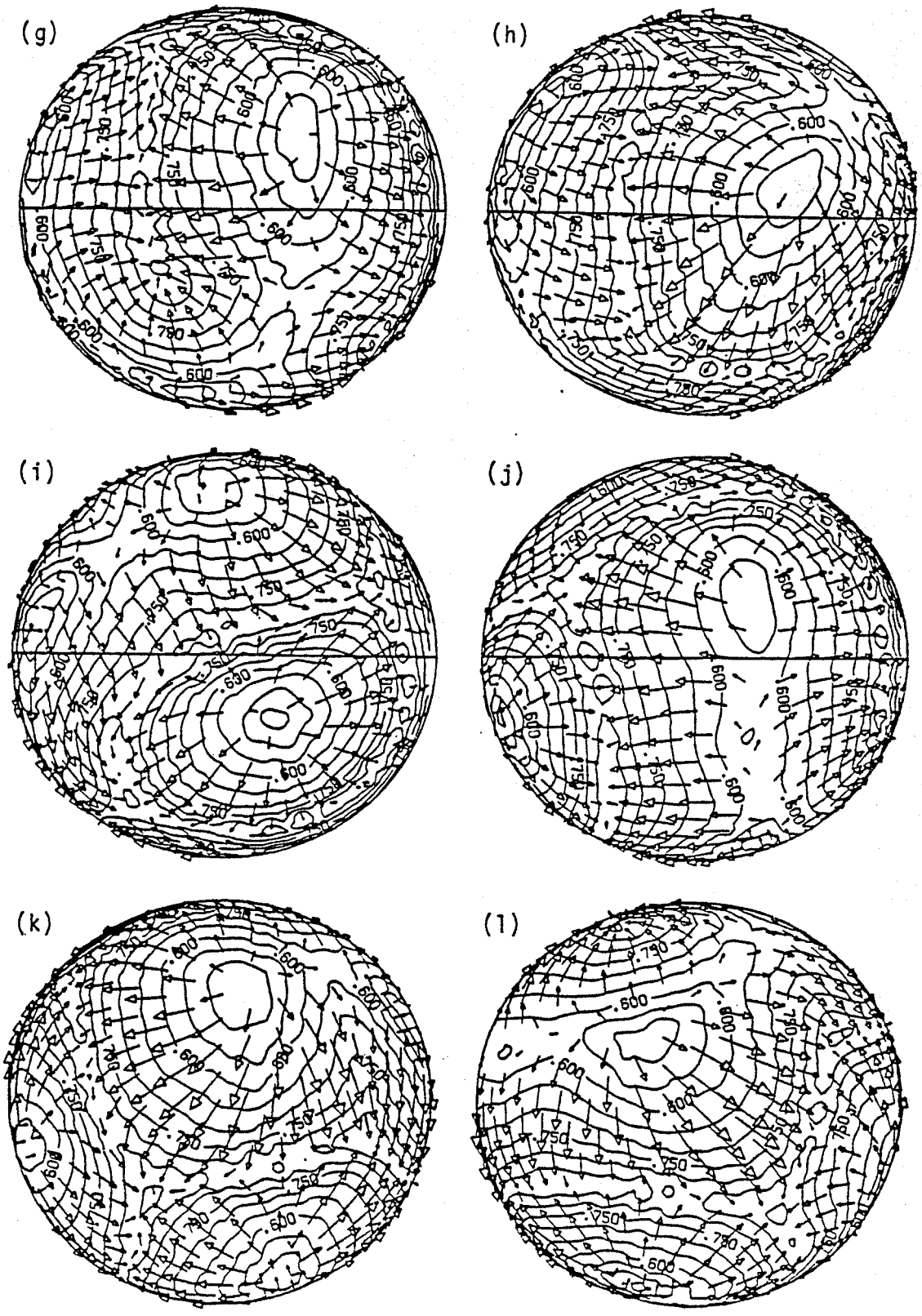

Figure 8.8

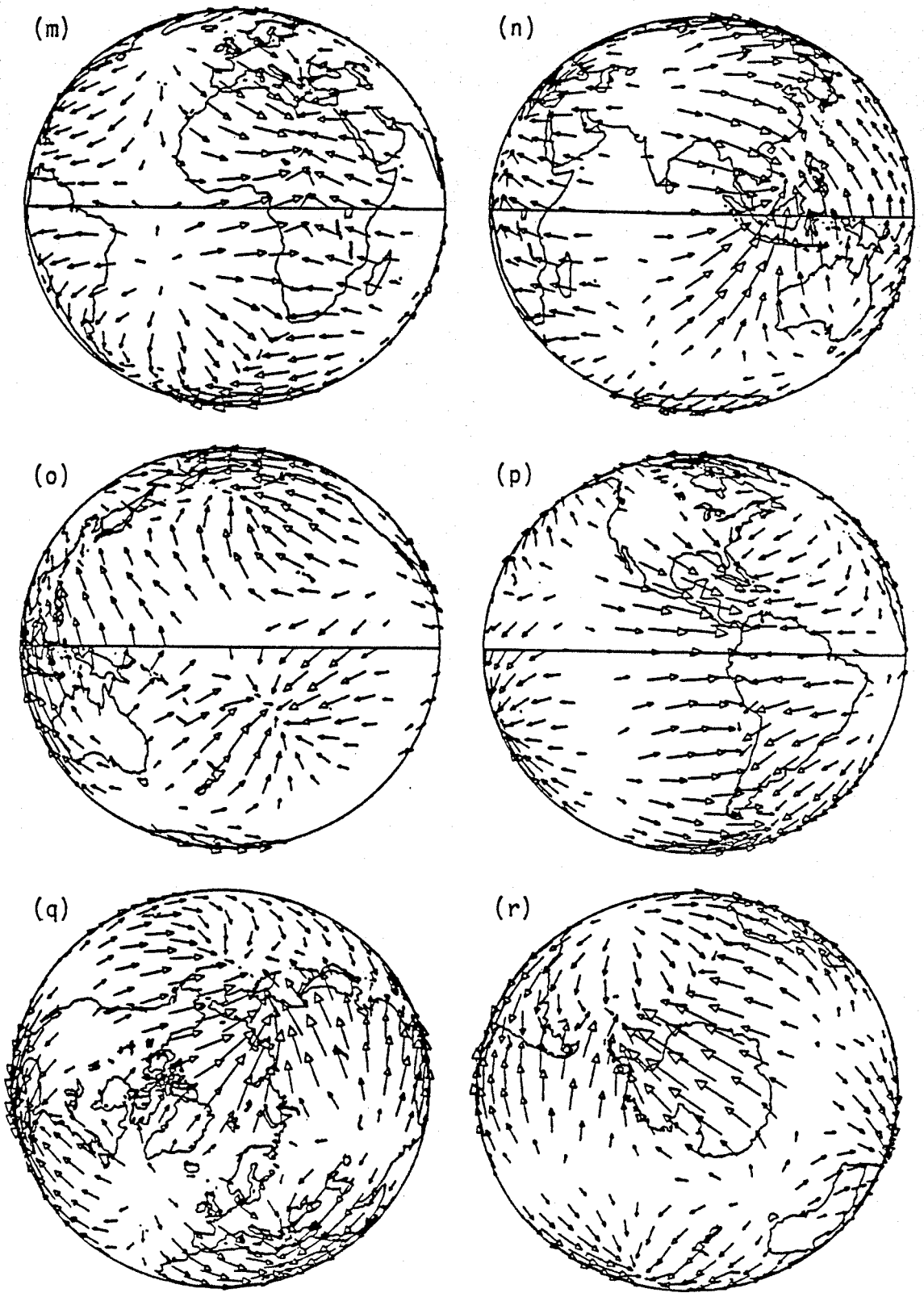

Figure 8.8

Figure 8.9. Same solution as Figure 8.6 except at approximately 3.3 convective overturn times. Maximum velocity for views (a)-(f) is 1.29 mm/yr, for views (g)-(l) is 2.29 mm/yr, and for views (m)-(r) is 1.32 mm/yr. (s)-(x) have the same significance and normalization as (m)-(r) in Figure 8.1.

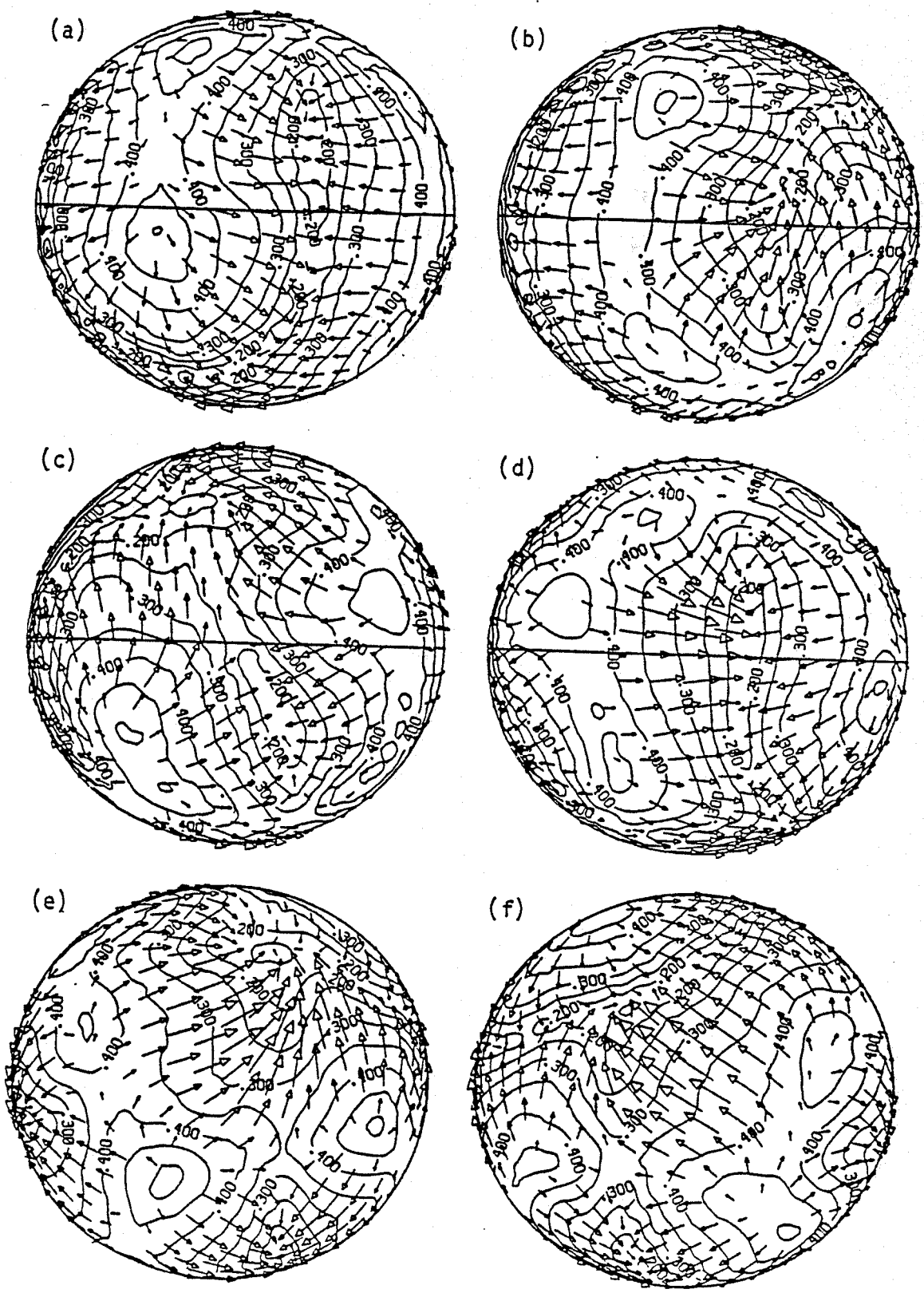

Figure 8.9

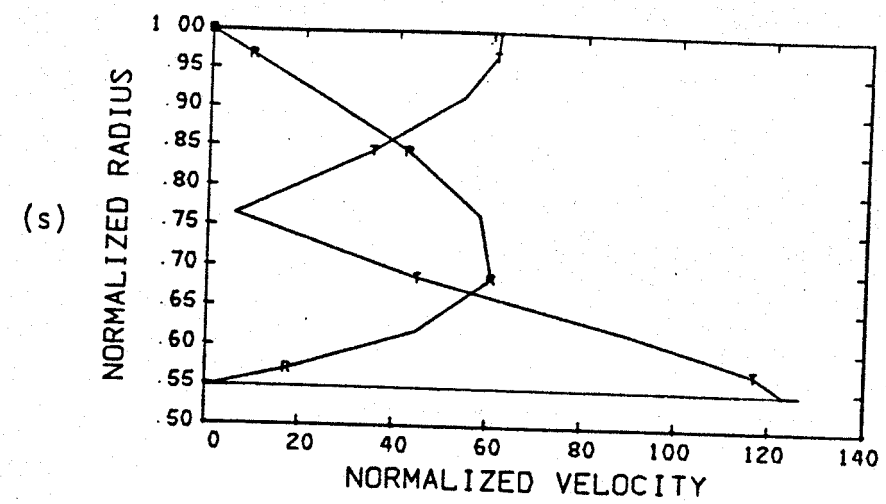
(s)
NORMALIZED RADIUS
1.00
.95
.90
.85
.80
.75
.70
.65
.60
.55
.50
0
20
40
60
80
100
120
140
NORMALIZED VELOCITY

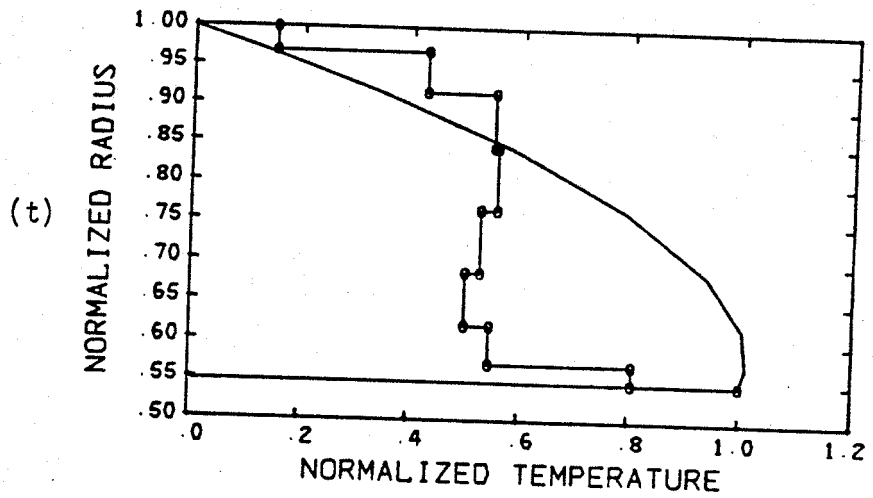
(t)
NORMALIZED RADIUS
1.00
.95
.90
.85
.80
.75
.70
.65
.60
.55
.50
0
.2
.4
.6
.8
1.0
1.2
NORMALIZED TEMPERATURE

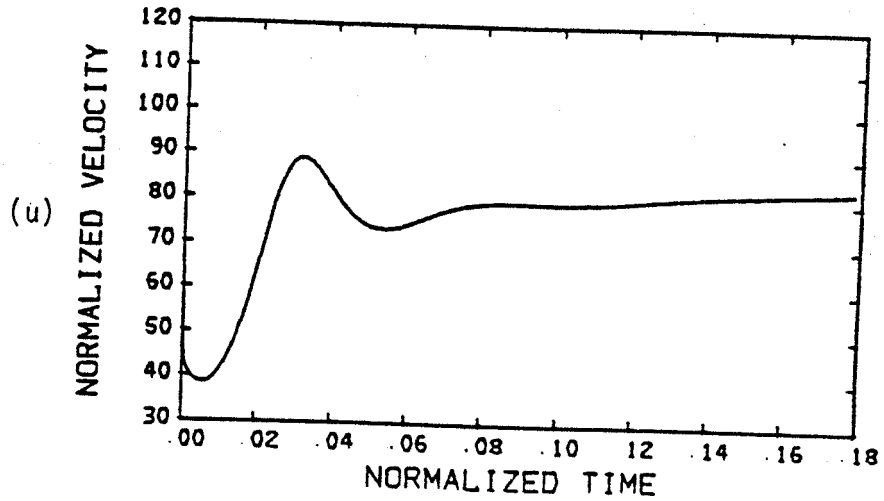
(u)
NORMALIZED VELOCITY
120
110
100
90
80
70
60
50
40
30
.00
.02
.04
.06
.08
.10
.12
.14
.16
.18
NORMALIZED TIME

Figure 8.9

(v)

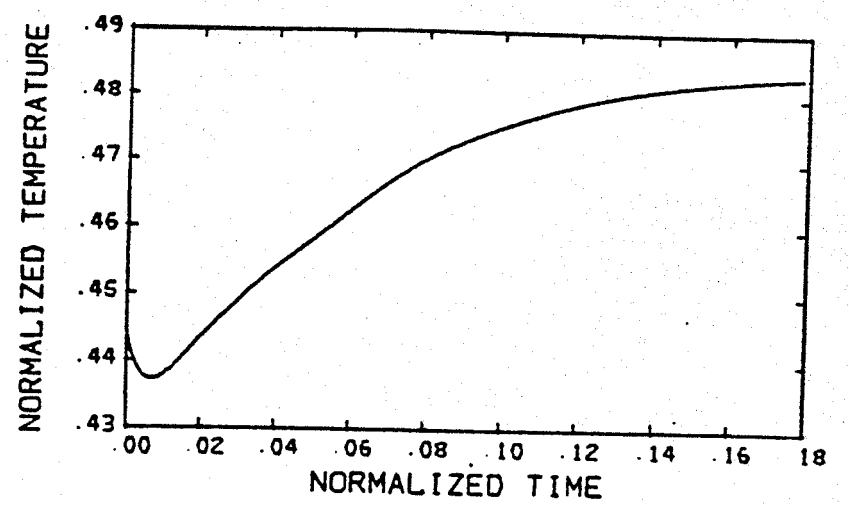

(w)

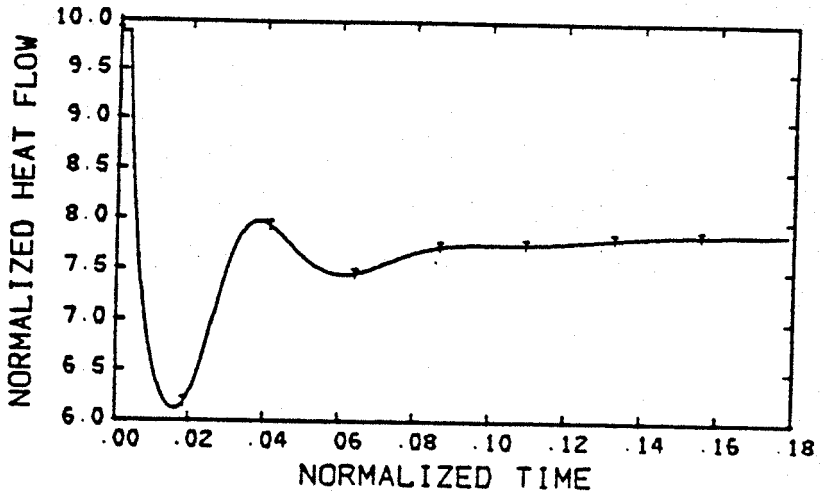

(x)

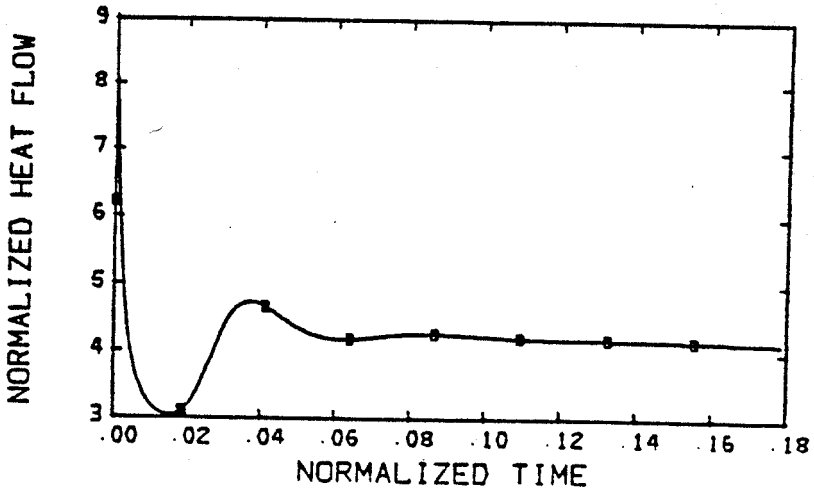

Figure 8.9

Figure 8.10. Convection solution after approximately 0.1 convective overturn time for spherical shell representing the earth's mantle, radius ratio 0.547, Rayleigh number 100,000, 48% internal heating, constant amplitude gravitational acceleration, initialized with warmer temperatures beneath present mid-ocean ridges and cooler temperatures adjacent to ocean trenches. Velocity and temperature fields are shown in (a)-(l). Orientations and radial positions of views and normalization of temperature contours are identical to views (a)-(l) of Figure 8.2. Maximum velocity for views (a)-(f) is 2.42 mm/yr and for views (g)-(l) is 4.10 mm/yr. Views (m)-(r) have the same orientation as (a)-(f) with radial position of 6368 km and maximum velocity of 2.43 mm/yr.

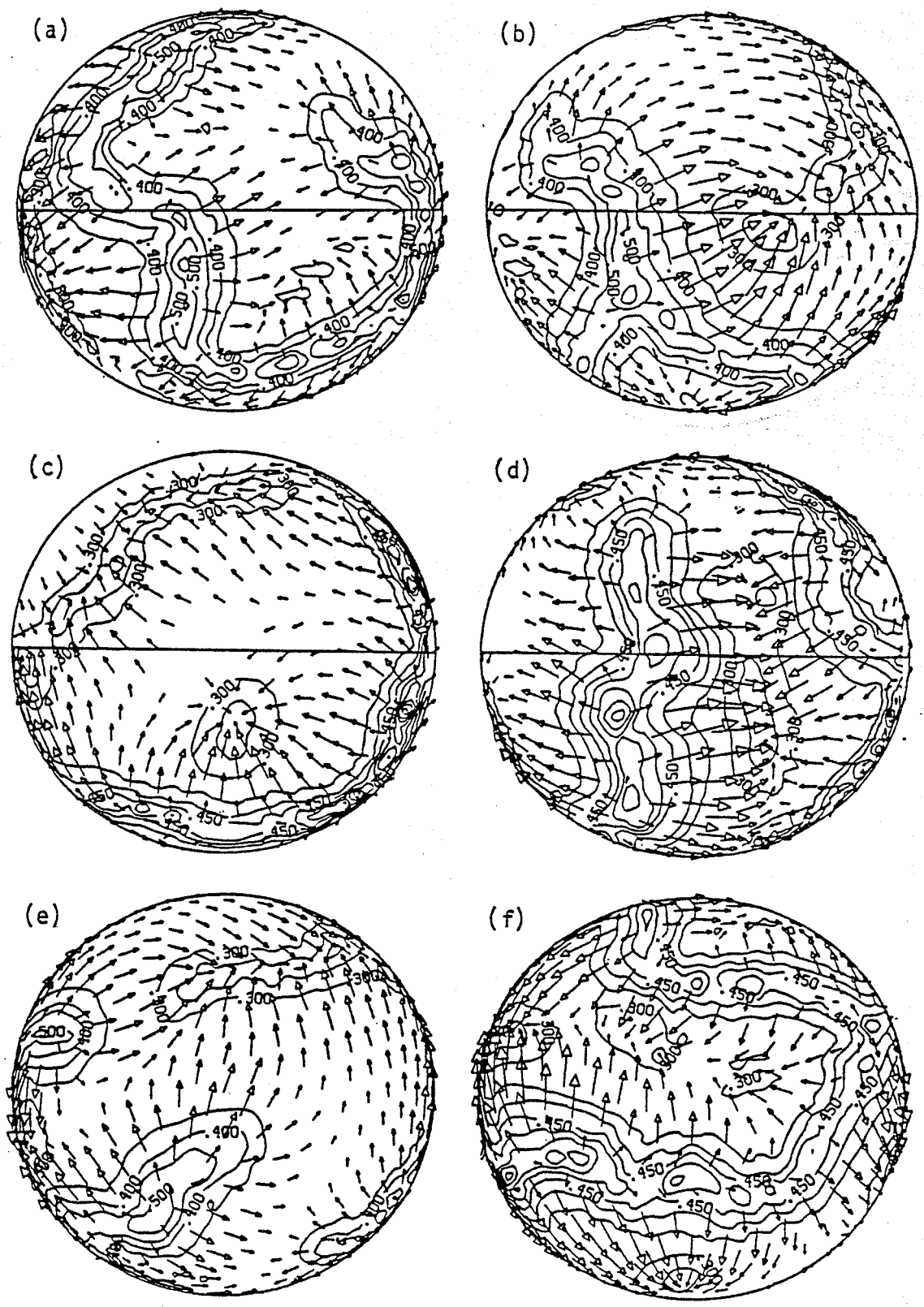

Figure 8.10

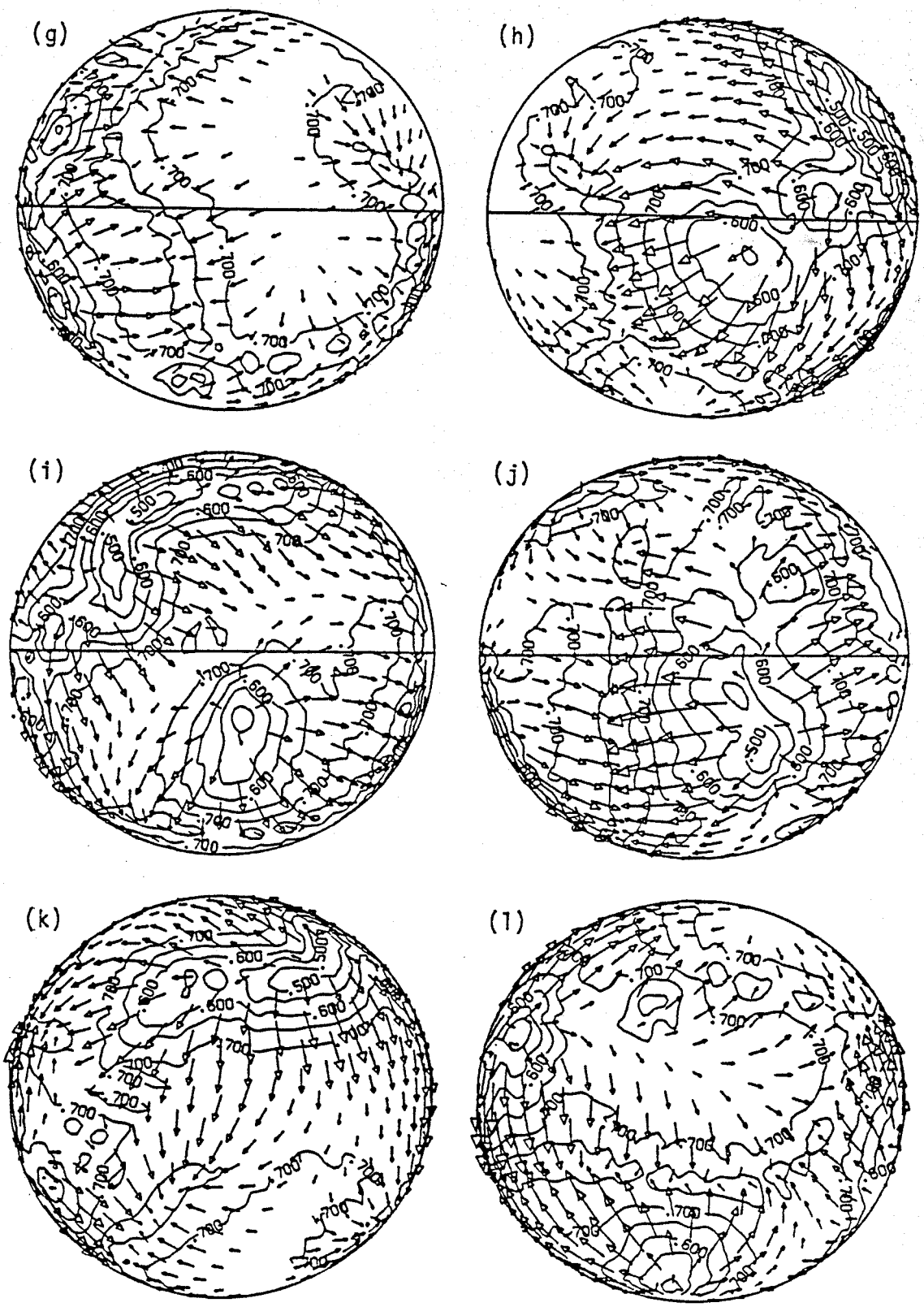

Figure 8.10

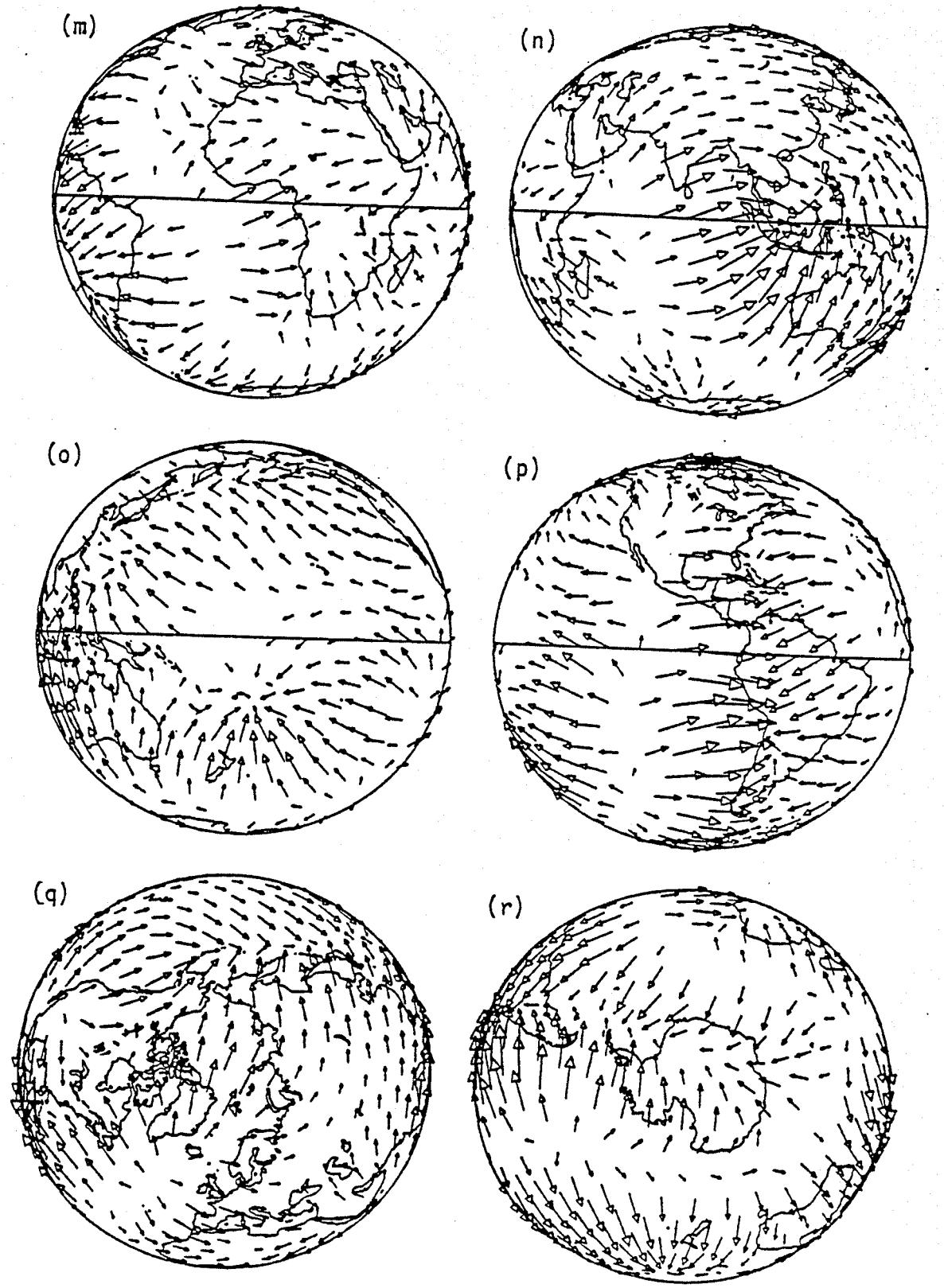

Figure 8.10

Figure 8.11. Same solution as Figure 8.10 except at approximately 0.9 overturn time. Maximum velocity for views (a)-(f) is 2.78 mm/yr, for views (g)-(l) is 4.59 mm/yr, and for views (m)-(r) is 2.81 mm/yr.

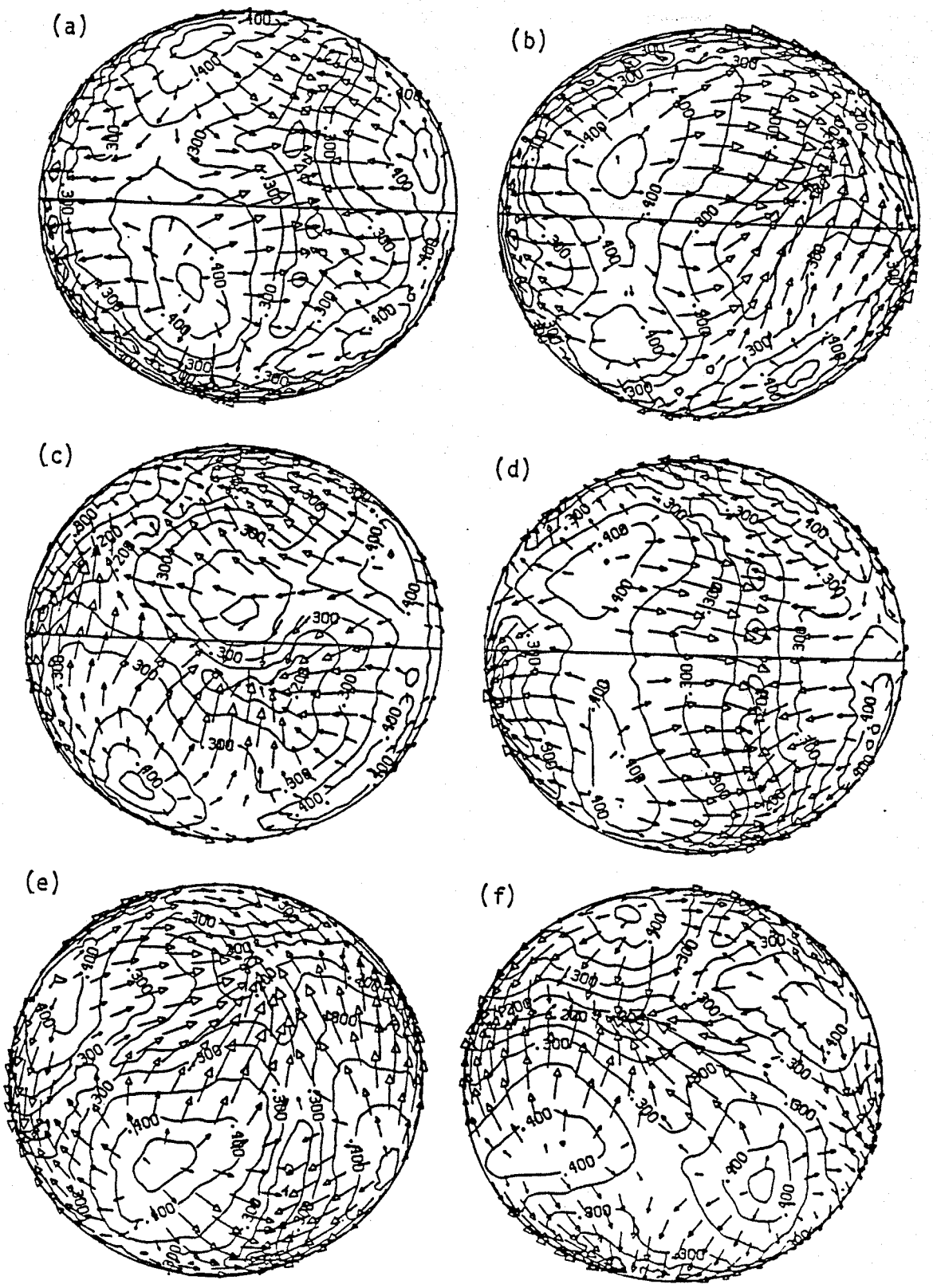

Figure 8.11

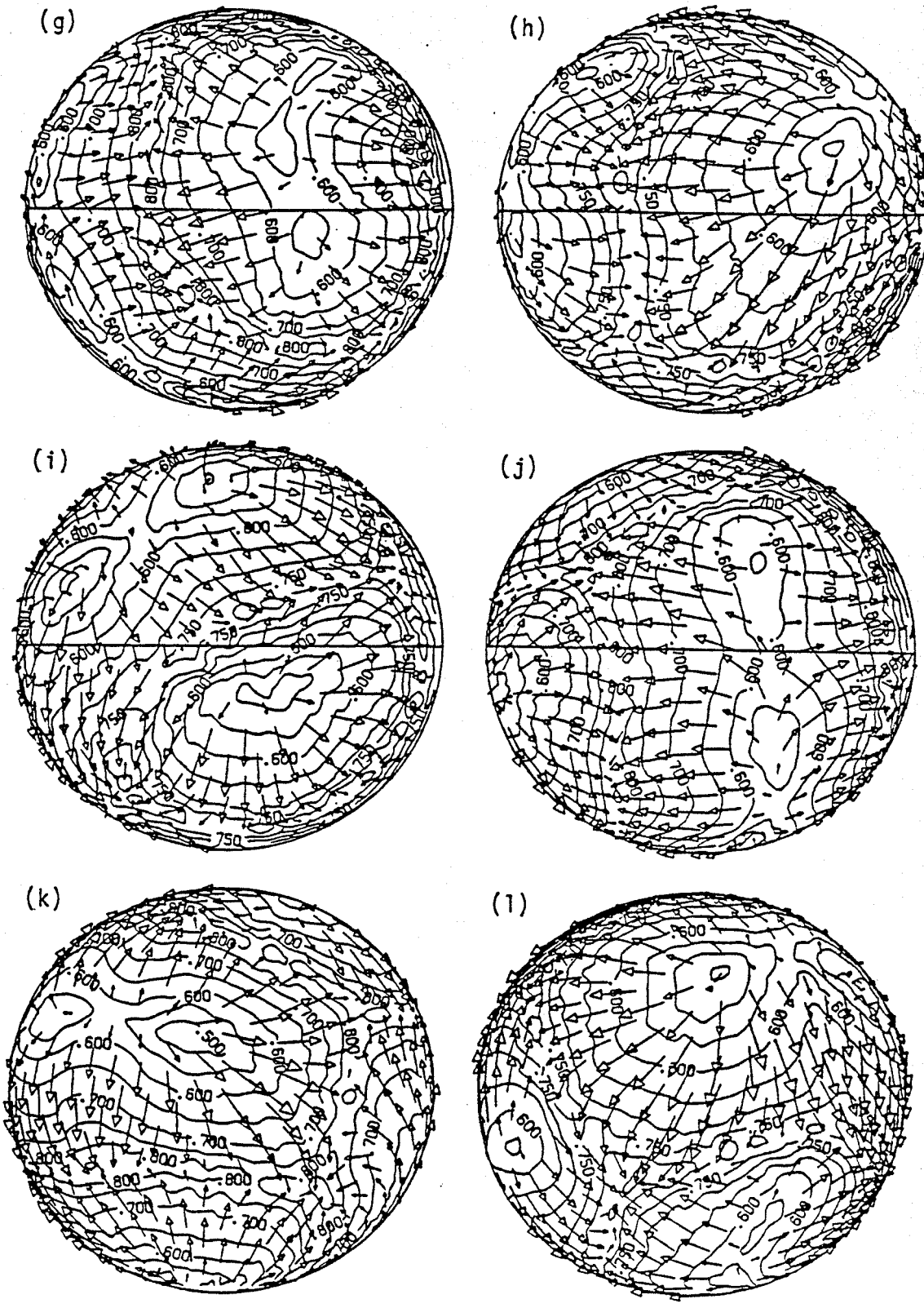

Figure 8.11

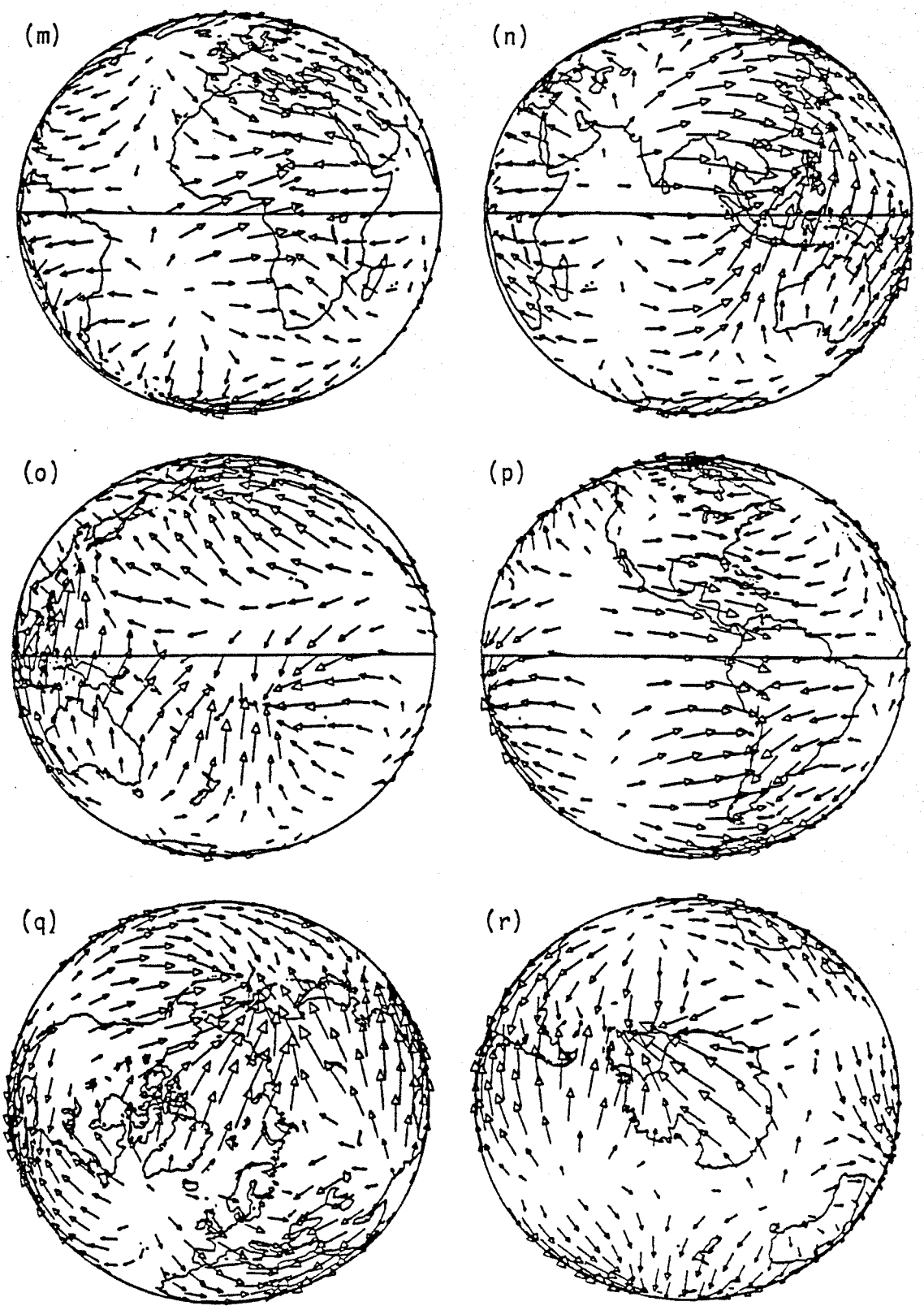

Figure 8.11

Figure 8.12. Same solution as Figure 8.10 except at approximately 2.3 convective overturn times. Maximum velocity for views (a)-(f) is 3.24 mm/yr, for views (g)-(l) is 5.69 mm/yr, and for views (m)-(r) is 3.28 mm/yr.

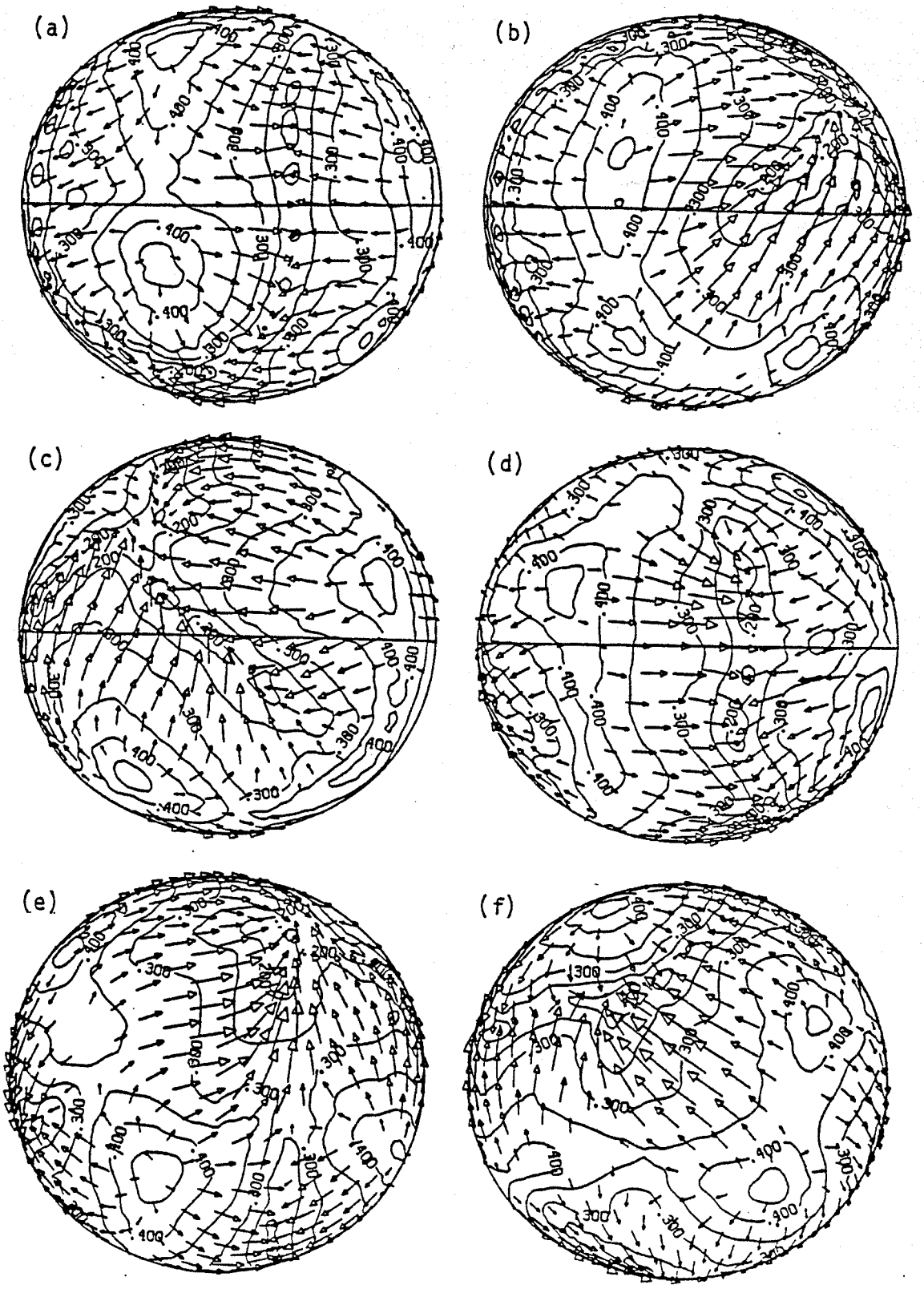

Figure 8.12

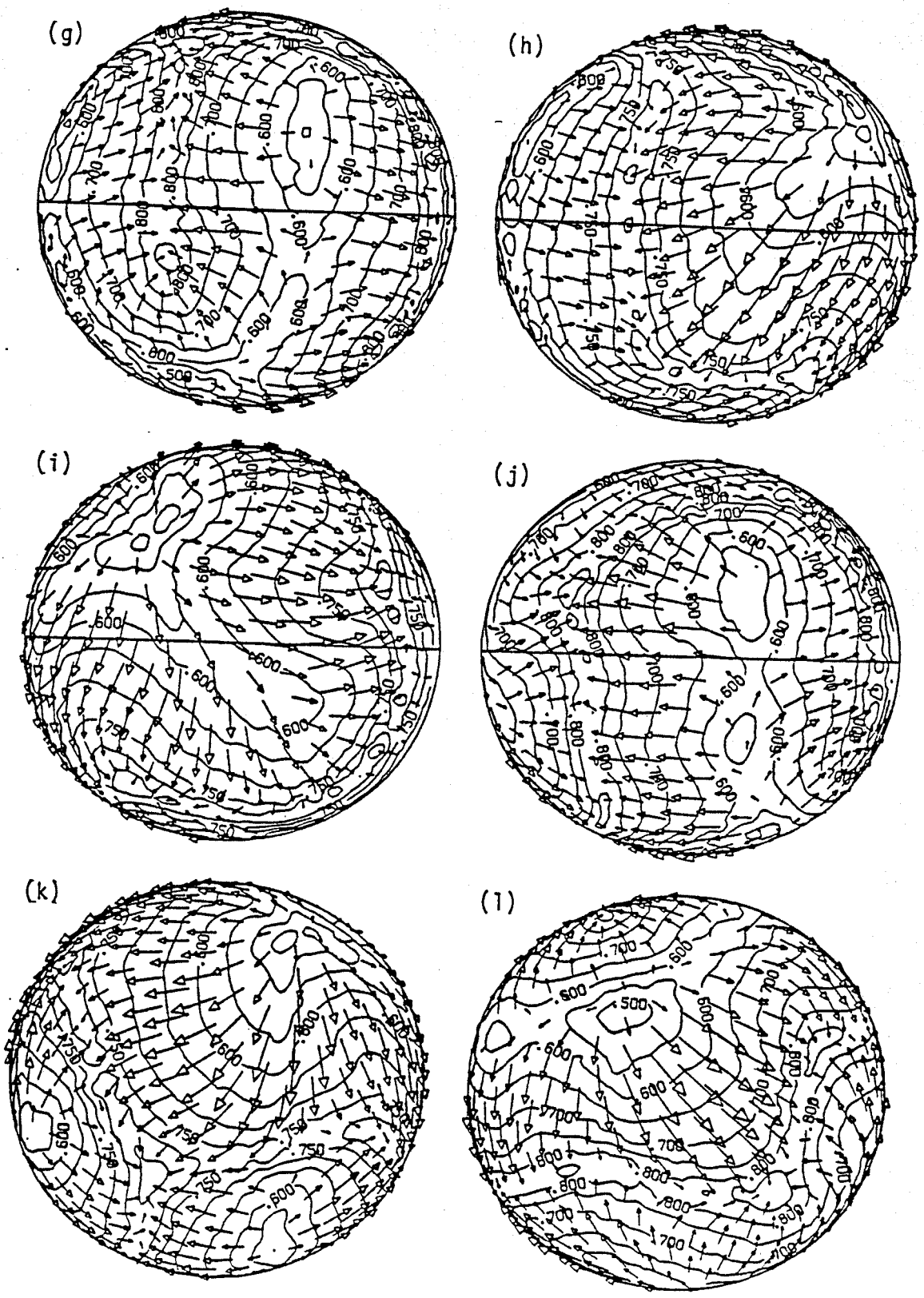

Figure 8.12

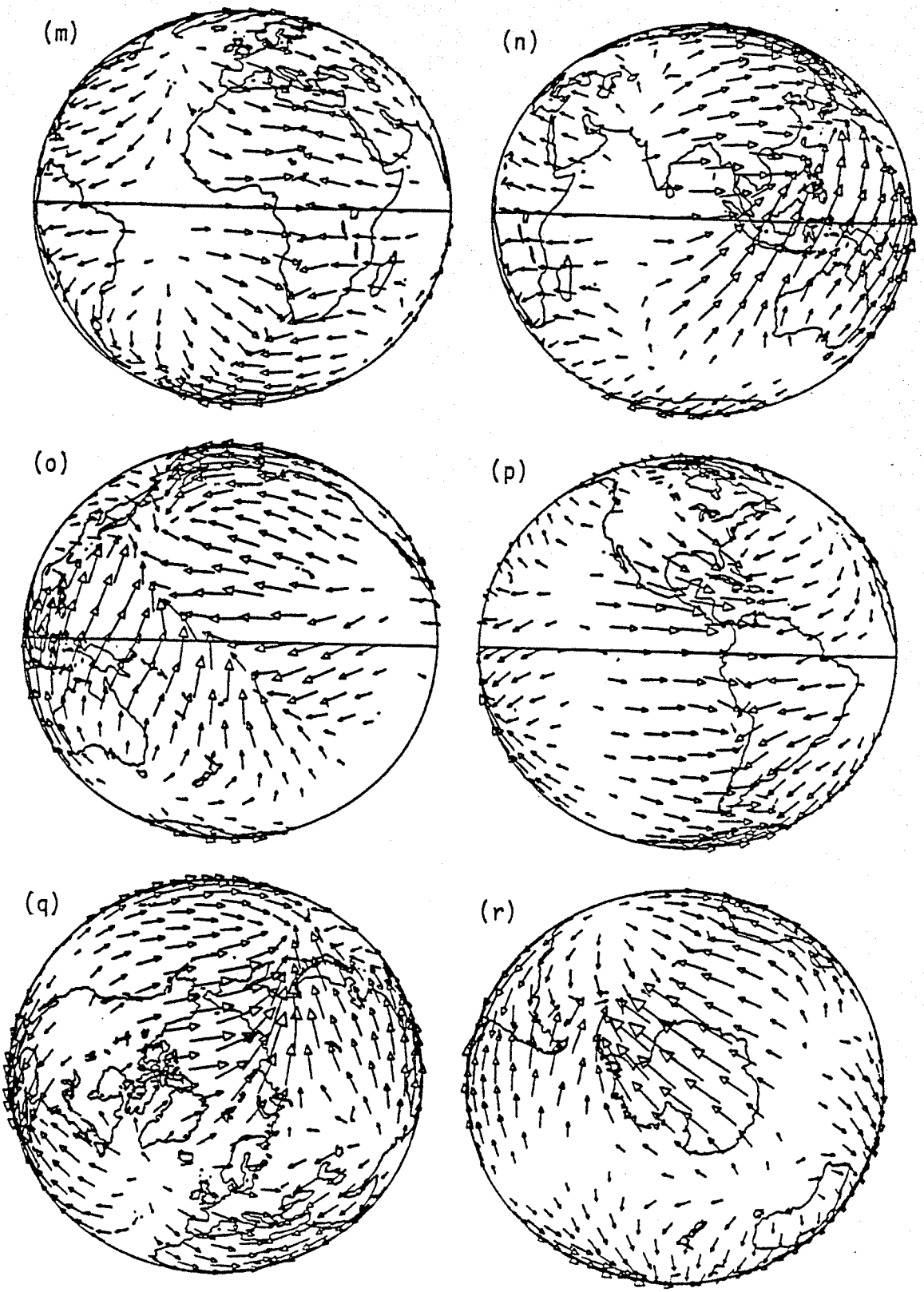

Figure 8.12

Figure 8.13. Same solution as Figure 8.10 except at approximately 3.0 convective overturn times. Maximum velocity for views (a)-(f) is 3.17 mm/yr, for views (g)-(l) is 5.58 mm/yr, and for views (m)-(r) is 3.19 mm/yr.

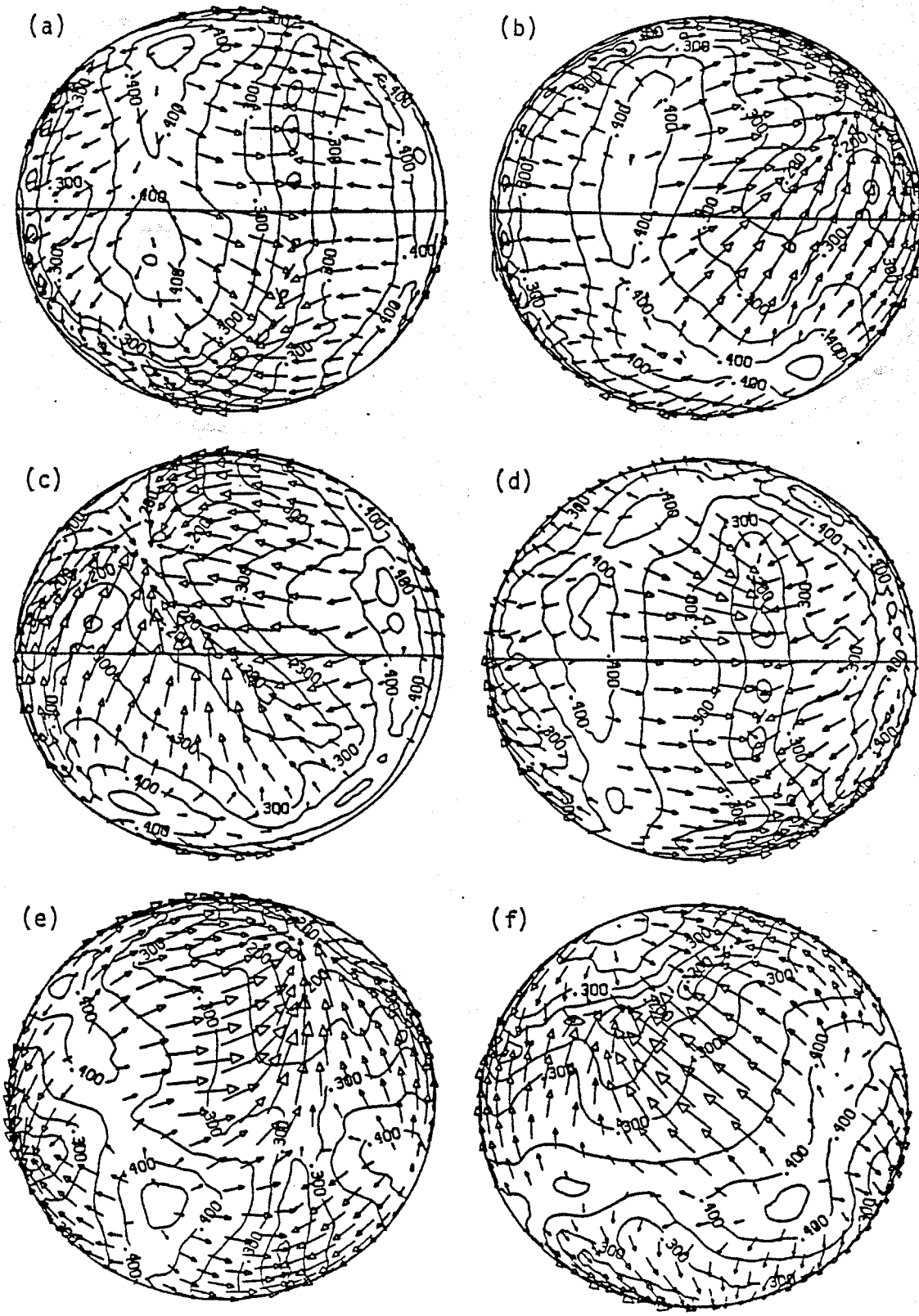

Figure 8.13

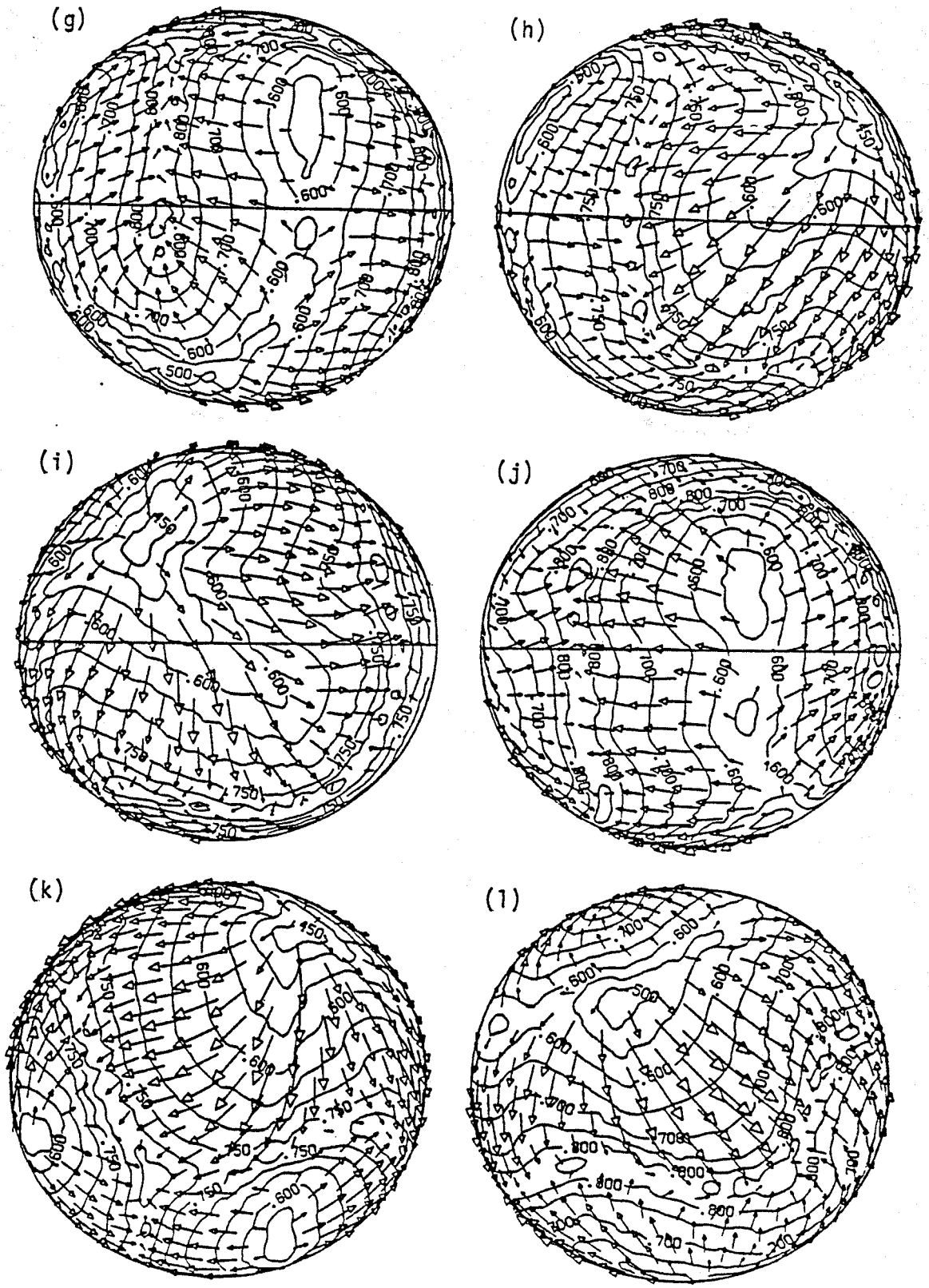

Figure 8.13

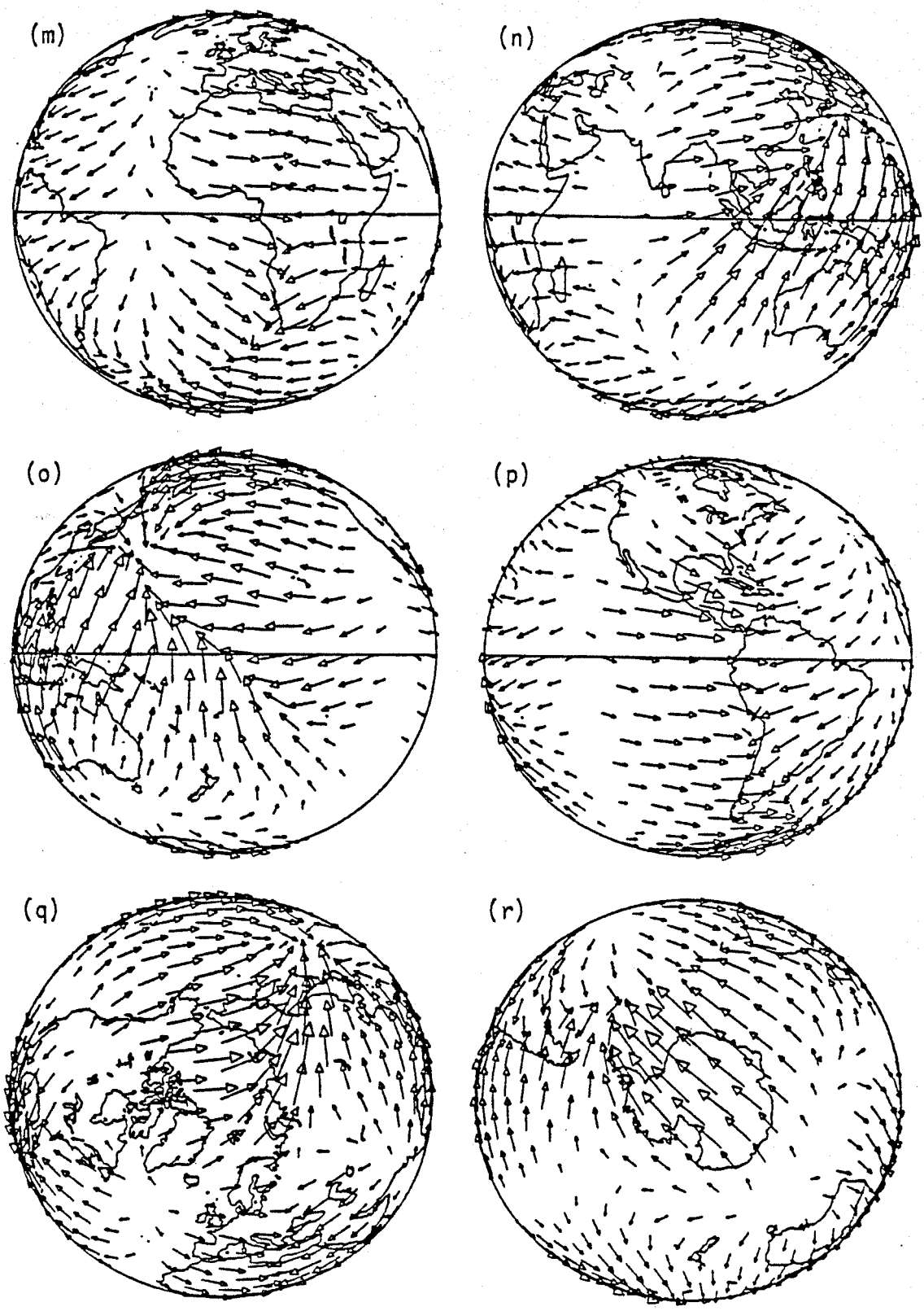

Figure 8.13

Figure 8.14. Same solution as Figure 8.10 except at approximately 4.0 convective overturn times. Maximum velocity for views (a)-(f) is 3.11 mm/yr, for views (g)-(l) is 5.61 mm/yr, and for views (m)-(r) is 3.12 mm/yr. (s)-(x) have the same significance and normalization as (m)-(r) in Figure 8.1.

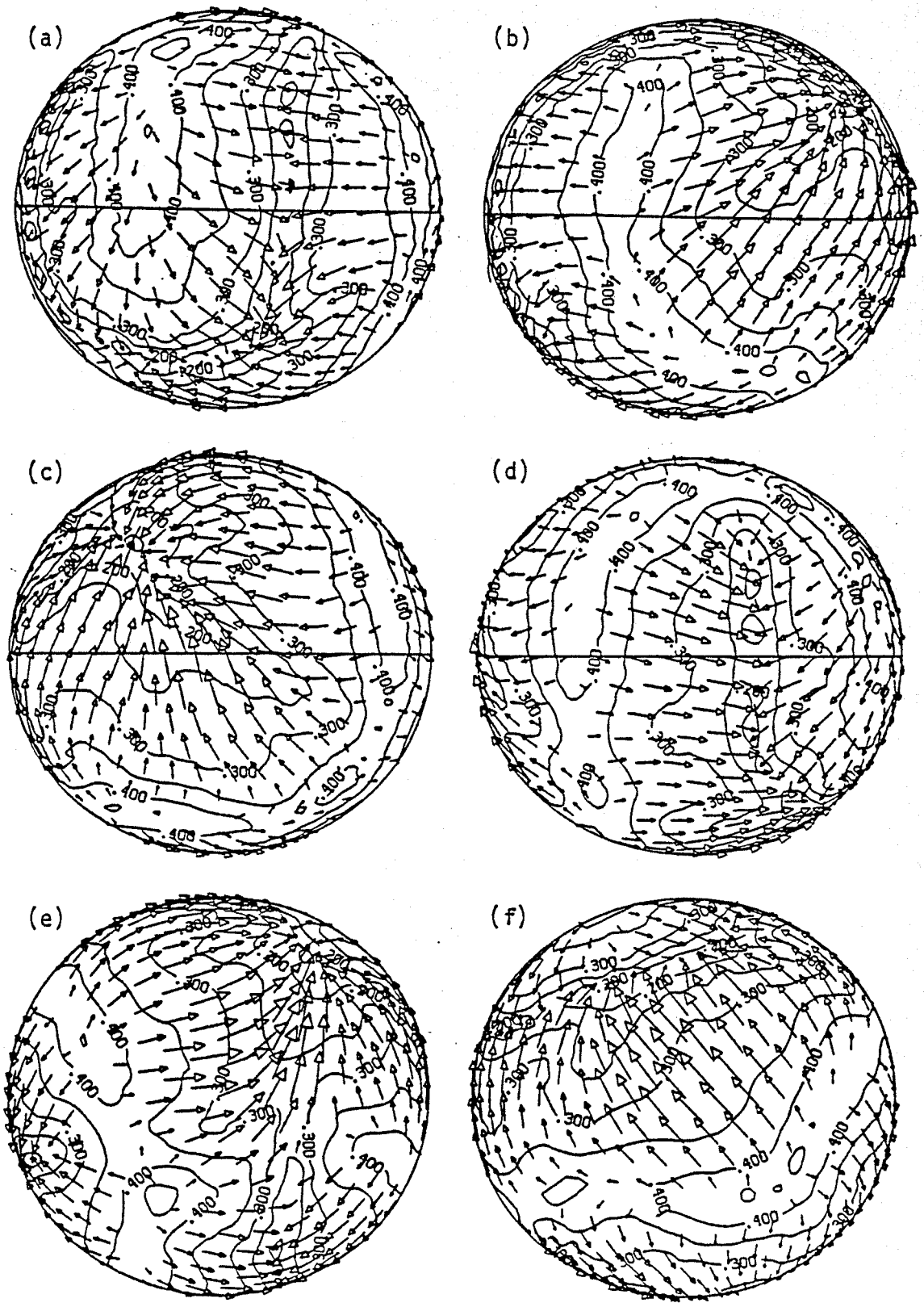

Figure 8.14

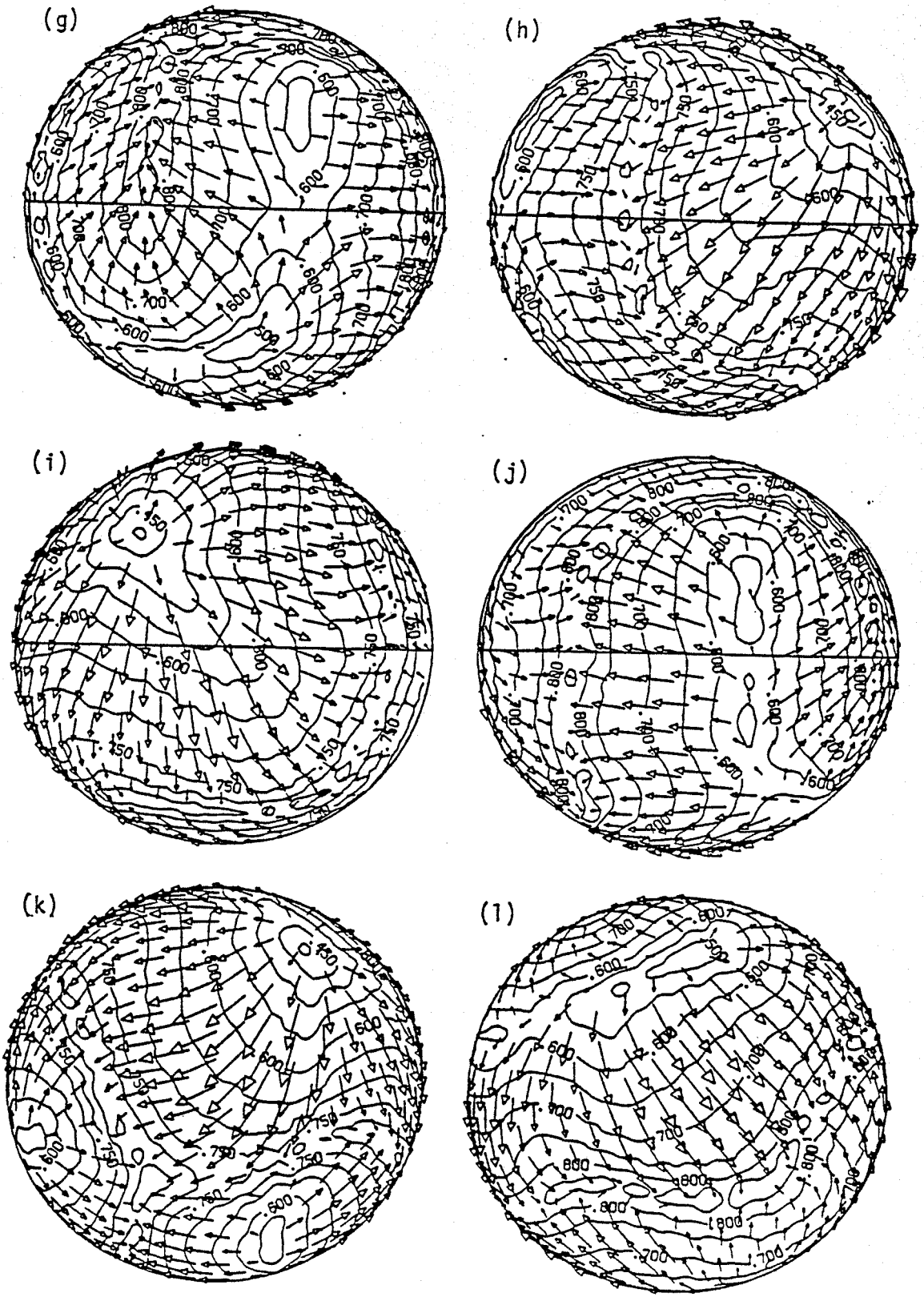

Figure 8.14

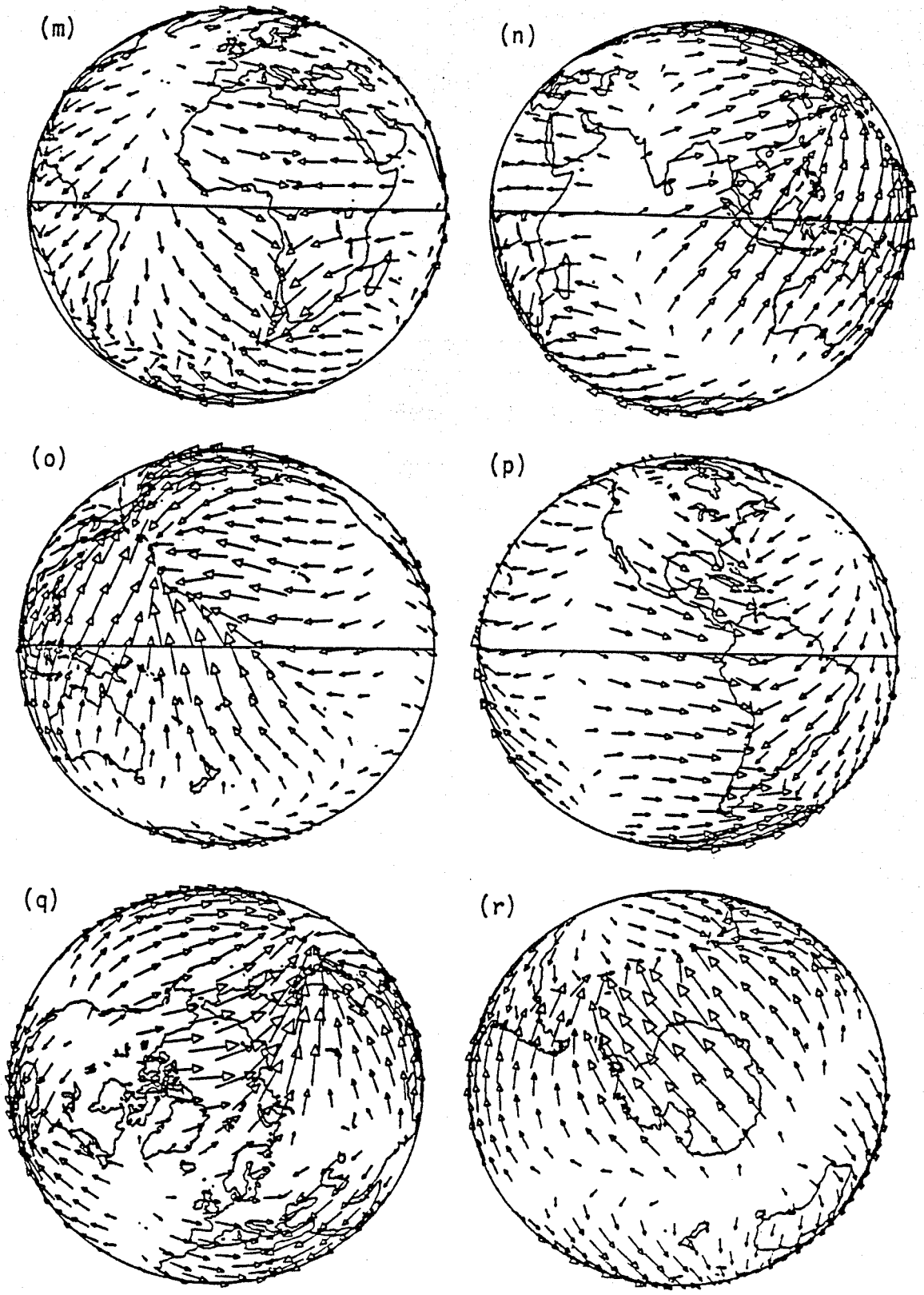

Figure 8.14

(s)

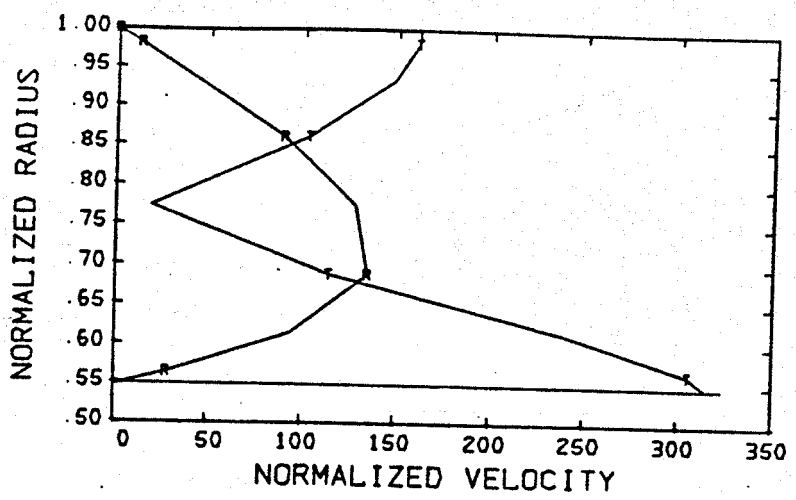

(t)

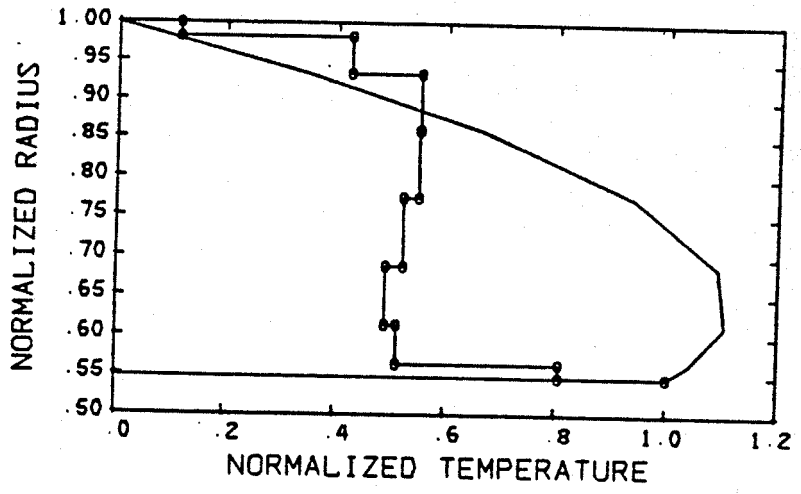

(u)

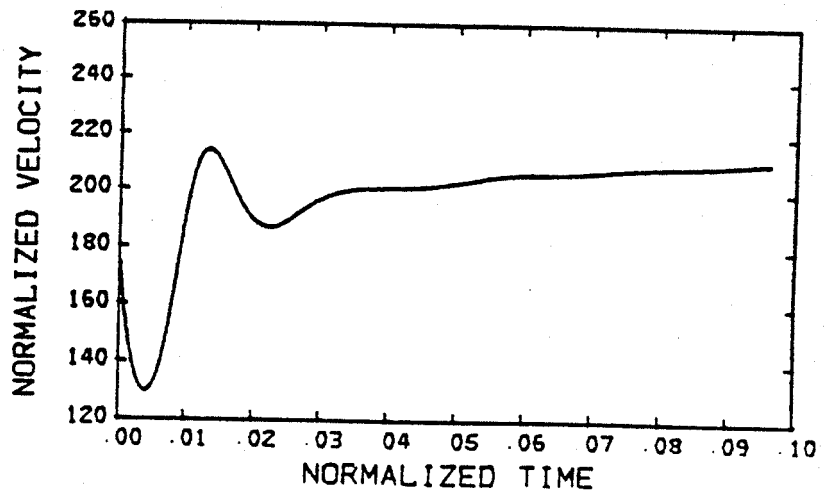

Figure 8.14

(v)

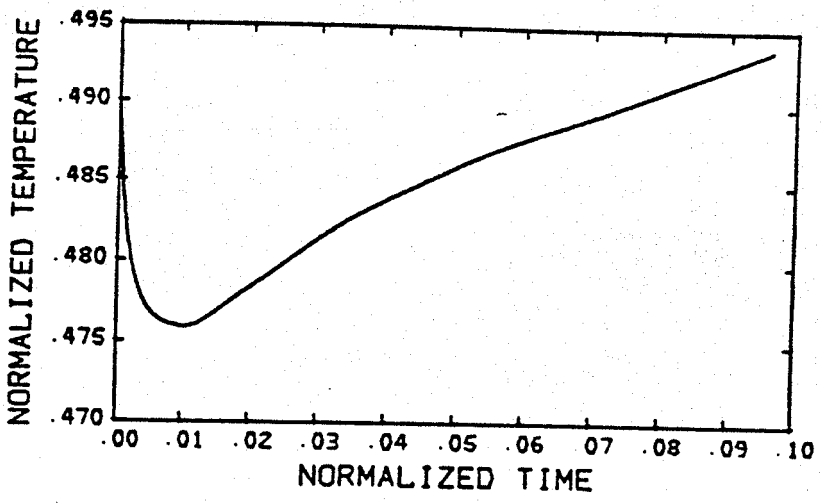

(w)

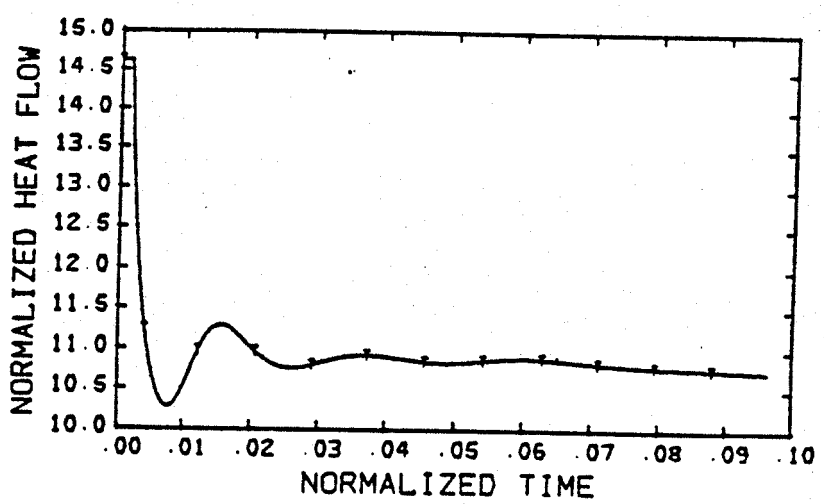

(x)

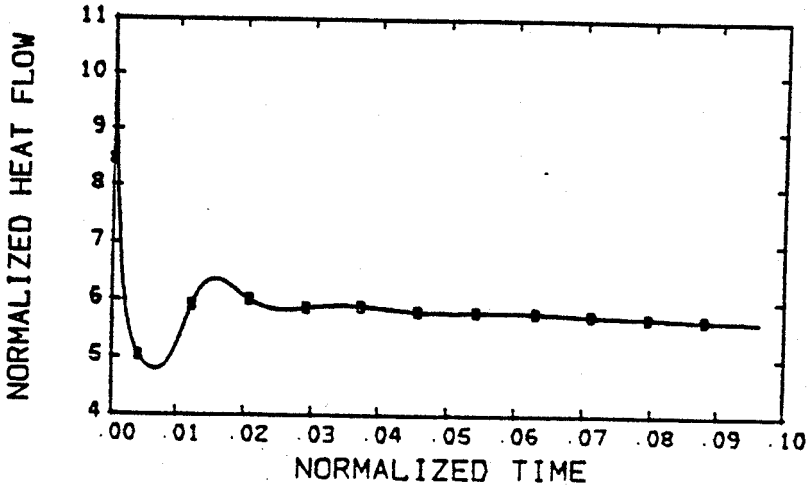

Figure 8.14

Figure 8.15. Convection solution after approximately 0.9 convective overturn time for spherical shell representing the earth's mantle, radius ratio 0.547, Rayleigh number 1,000,000, 48% internal heating, constant amplitude gravitational acceleration, initialized with warmer temperatures beneath present mid-ocean ridges and cooler temperatures adjacent to ocean trenches. Velocity and temperature fields are shown in (a)-(l). Orientations of views and normalization of temperature contours are identical to views (a)-(l) of Figure 8.1. Radial position for views (a)-(f) is 6340 km, and maximum velocity is 13.9 mm/yr. Radial position for views (g)-(l) is 3513 km, and maximum velocity is 20.4 mm/yr.

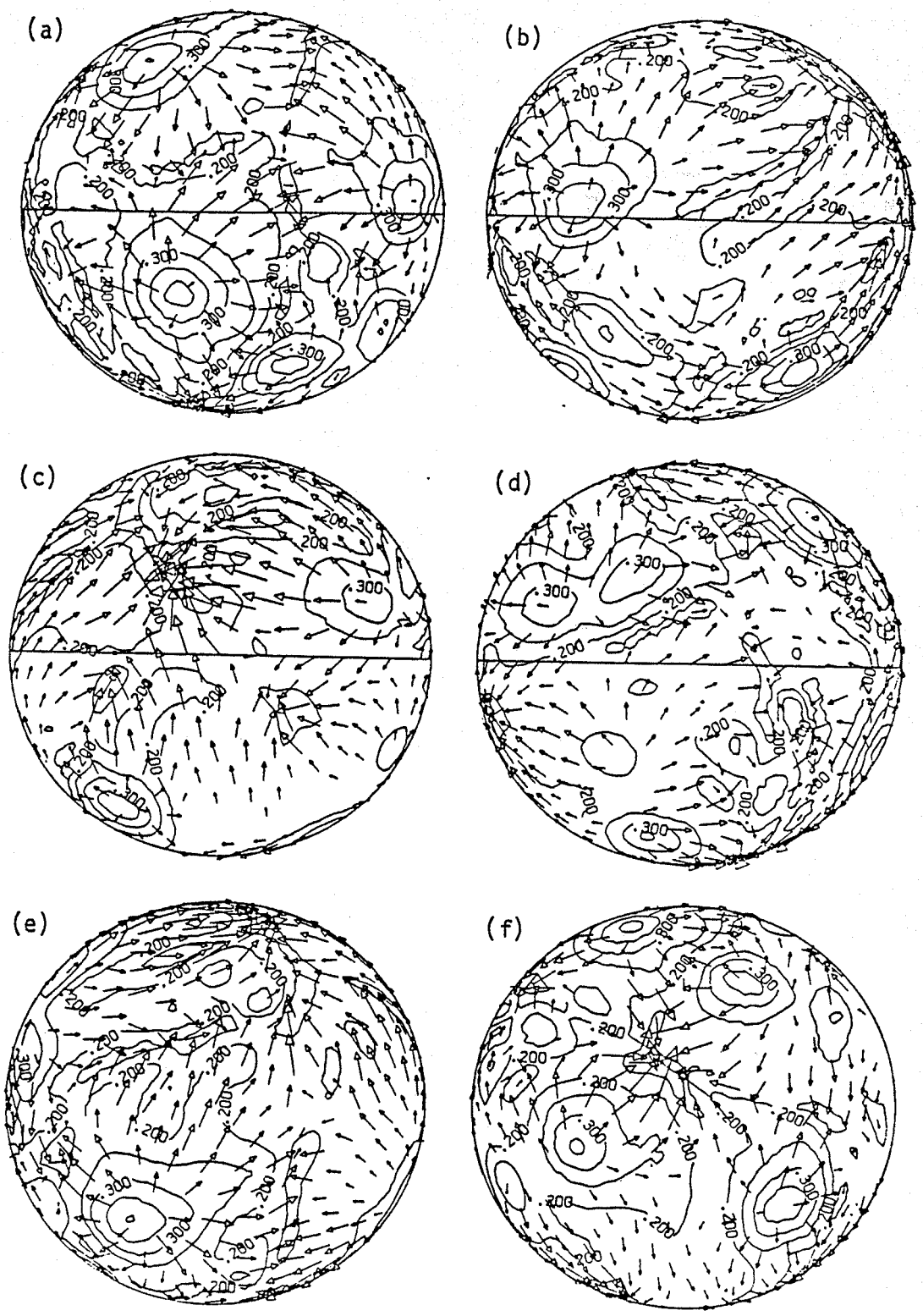

Figure 8.15

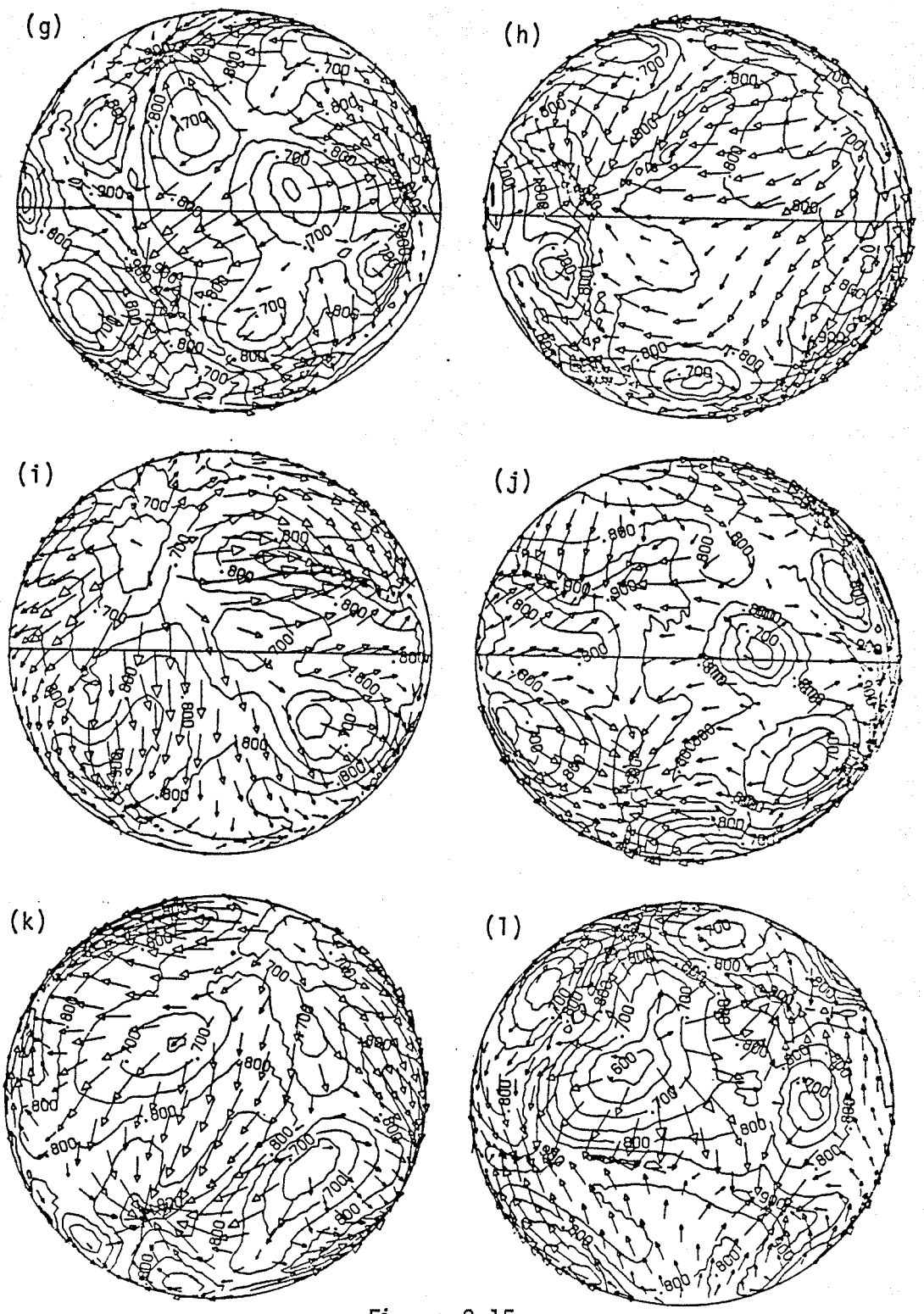

Figure 8.15

Figure 8.16. Same solution as Figure 8.15 except at approximately 1.8 overturn times. Maximum velocity for views (a)-(f) is 12.6 mm/yr and for views (g)-(l) is 17.1 mm/yr. (m)-(r) have the same significance and normalization as in Figure 8.1.

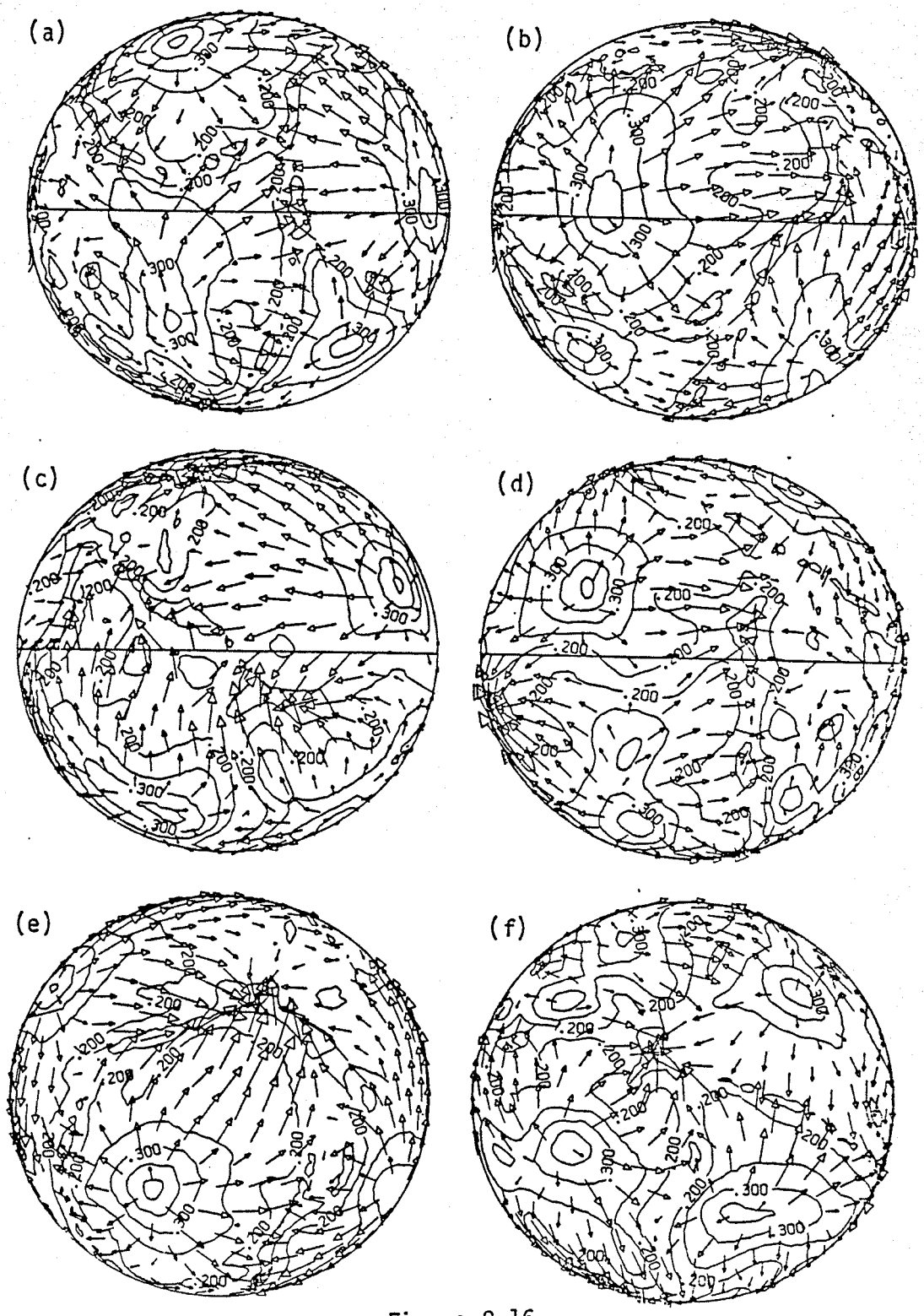

Figure 8.16

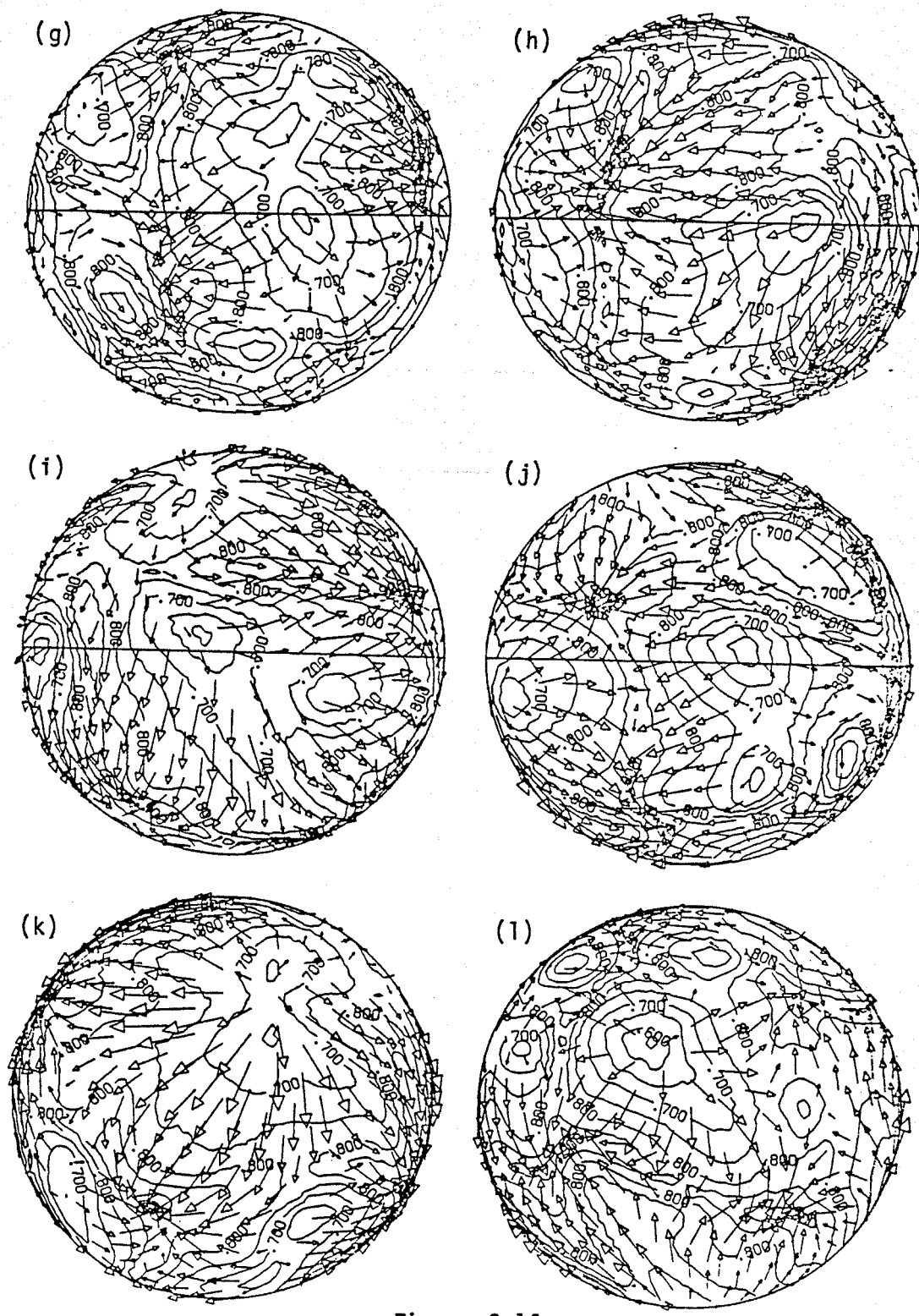

Figure 8.16

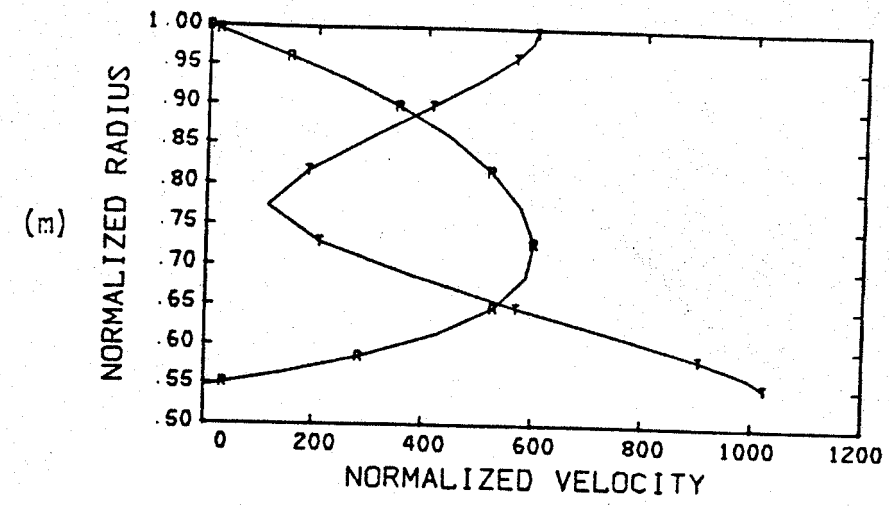
(m)
NORMALIZED RADIUS
1.00
.95
.90
.85
.80
.75
.70
.65
.60
.55
.50
0
200
400
600
800
1000
1200
NORMALIZED VELOCITY

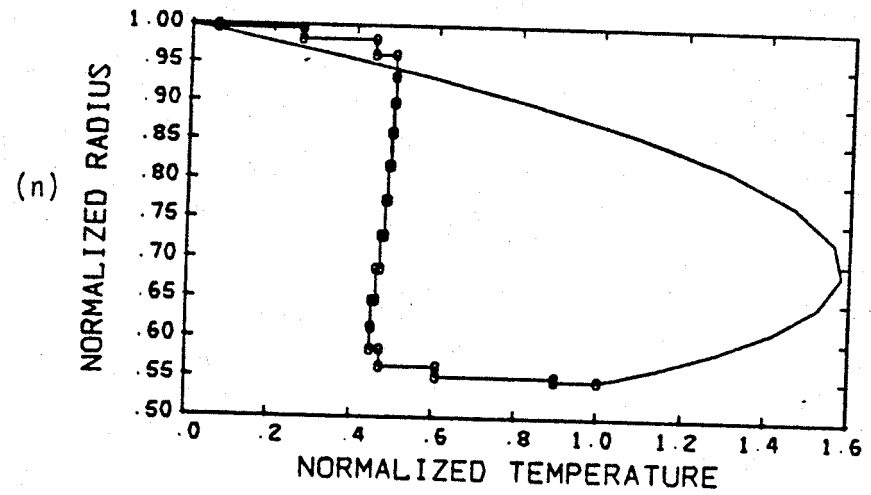
(n)
NORMALIZED RADIUS
1.00
.95
.90
.85
.80
.75
.70
.65
.60
.55
.50
.0
.2
.4
.6
.8
1.0
1.2
1.4
1.6
NORMALIZED TEMPERATURE

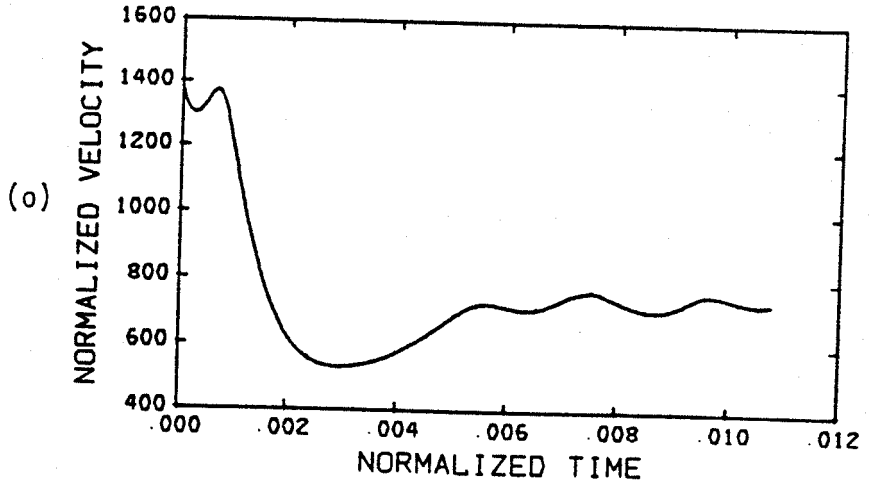
(o)
NORMALIZED VELOCITY
1600
1400
1200
1000
800
600
400
.000
.002
.004
.006
.008
.010
.012
NORMALIZED TIME

Figure 8.16

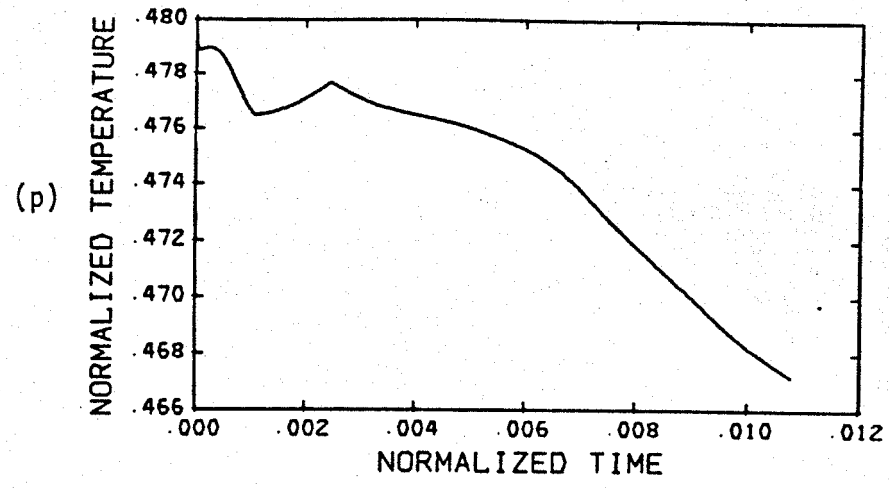
(p)
NORMALIZED TEMPERATURE
.480
.478
.476
.474
.472
.470
.468
.466
.000
.002
.004
.006
.008
.010
.012
NORMALIZED TIME

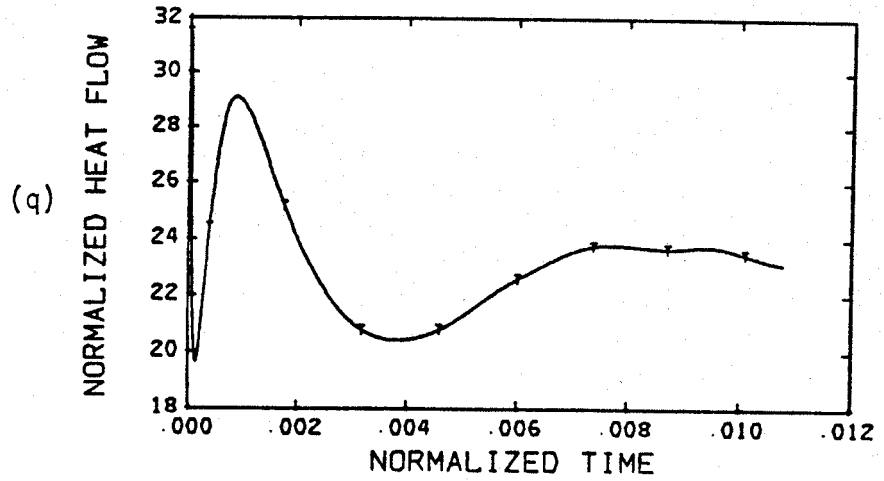
(q)
NORMALIZED HEAT FLOW
32
30
28
26
24
22
20
18
.000
.002
.004
.006
.008
.010
.012
NORMALIZED TIME

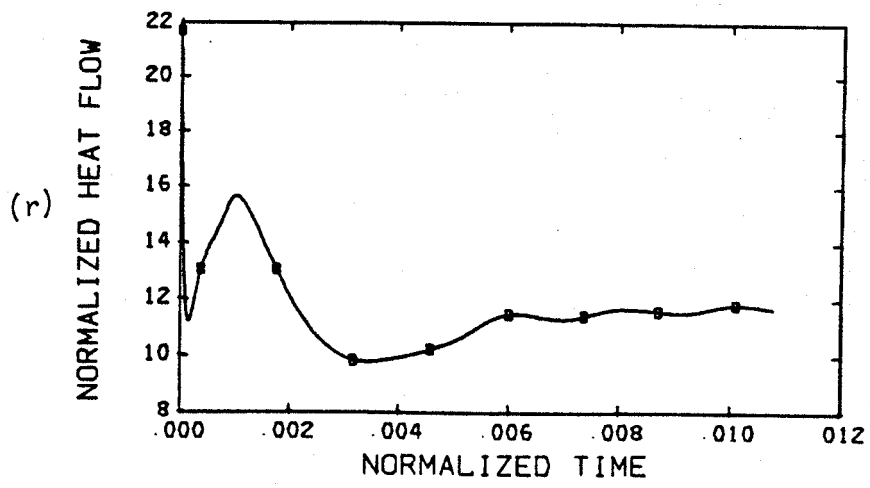
(r)
NORMALIZED HEAT FLOW
22
20
18
16
14
12
10
8
.000
.002
.004
.006
.008
.010
012
NORMALIZED TIME

Figure 8.16

Figure 8.17. Convection solution after approximately 0.1 convective overturn time for spherical shell representing the earth's mantle, radius ratio 0.547, Rayleigh number 1,000,000, 48% internal heating, constant amplitude gravitational acceleration, initialized with warmer temperatures beneath present mid-ocean ridges and cooler temperatures adjacent to ocean trenches. This case differs from that of Figures 8.15-8.16 in that it uses a different radial discretization. Cells in the outermost layer are 150 km in thickness as opposed to 28 km for the case of Figures 8.15-8.16. Velocity and temperature fields are shown in (a)-(l). Orientations of views and normalization of temperature contours are identical to views (a)-(l) of Figure 8.1. Radial position for views (a)-(f) is 6218 km, and maximum velocity is 25.2 mm/yr. Radial position for views (g)-(l) is 3520 km, and maximum velocity is 34.4 mm/yr. Views (m)-(r) have the same orientation as (a)-(f) with a radial position of 6368 km and maximum velocity of 25.5 mm/yr.

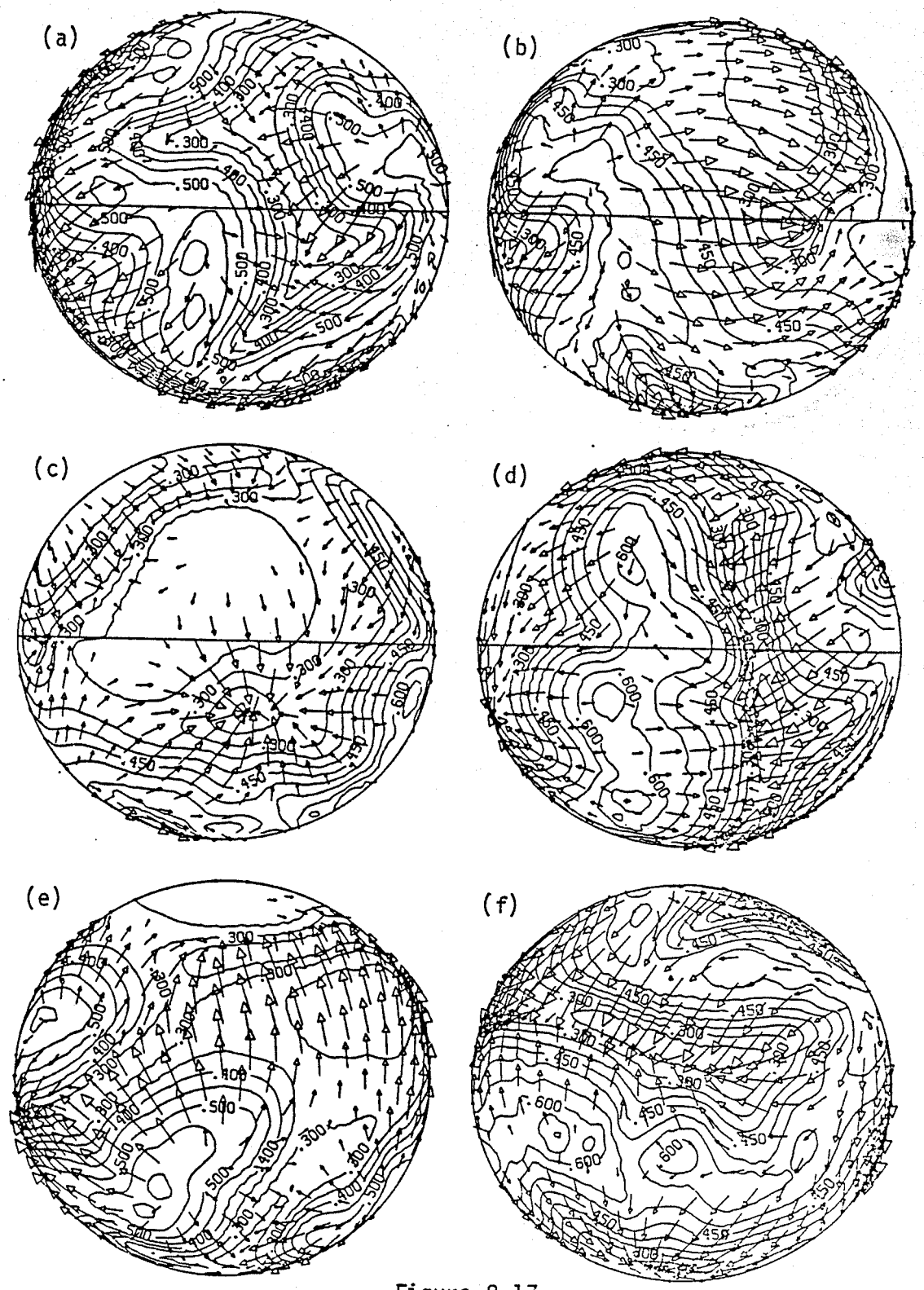

Figure 8.17

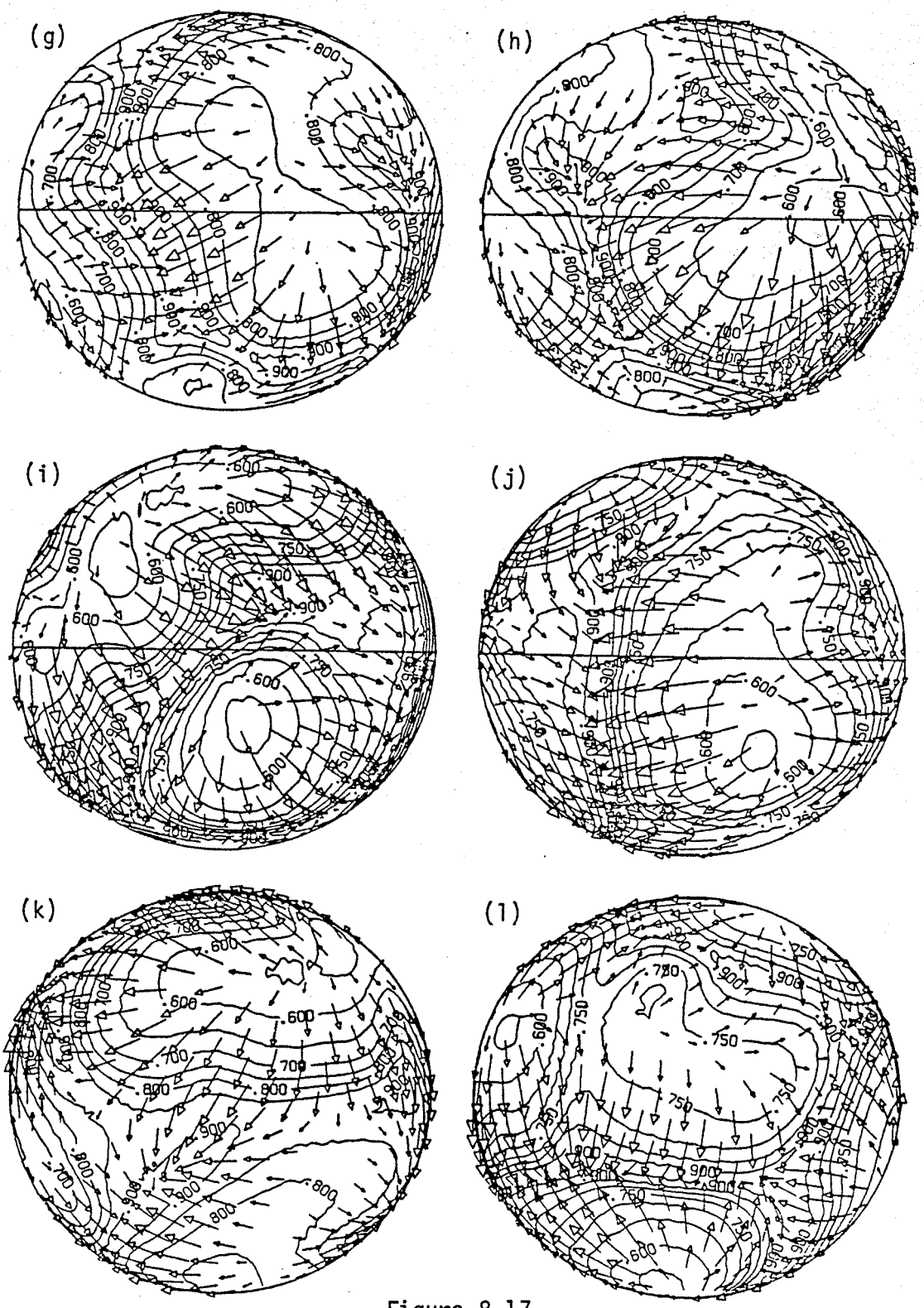

Figure 8.17

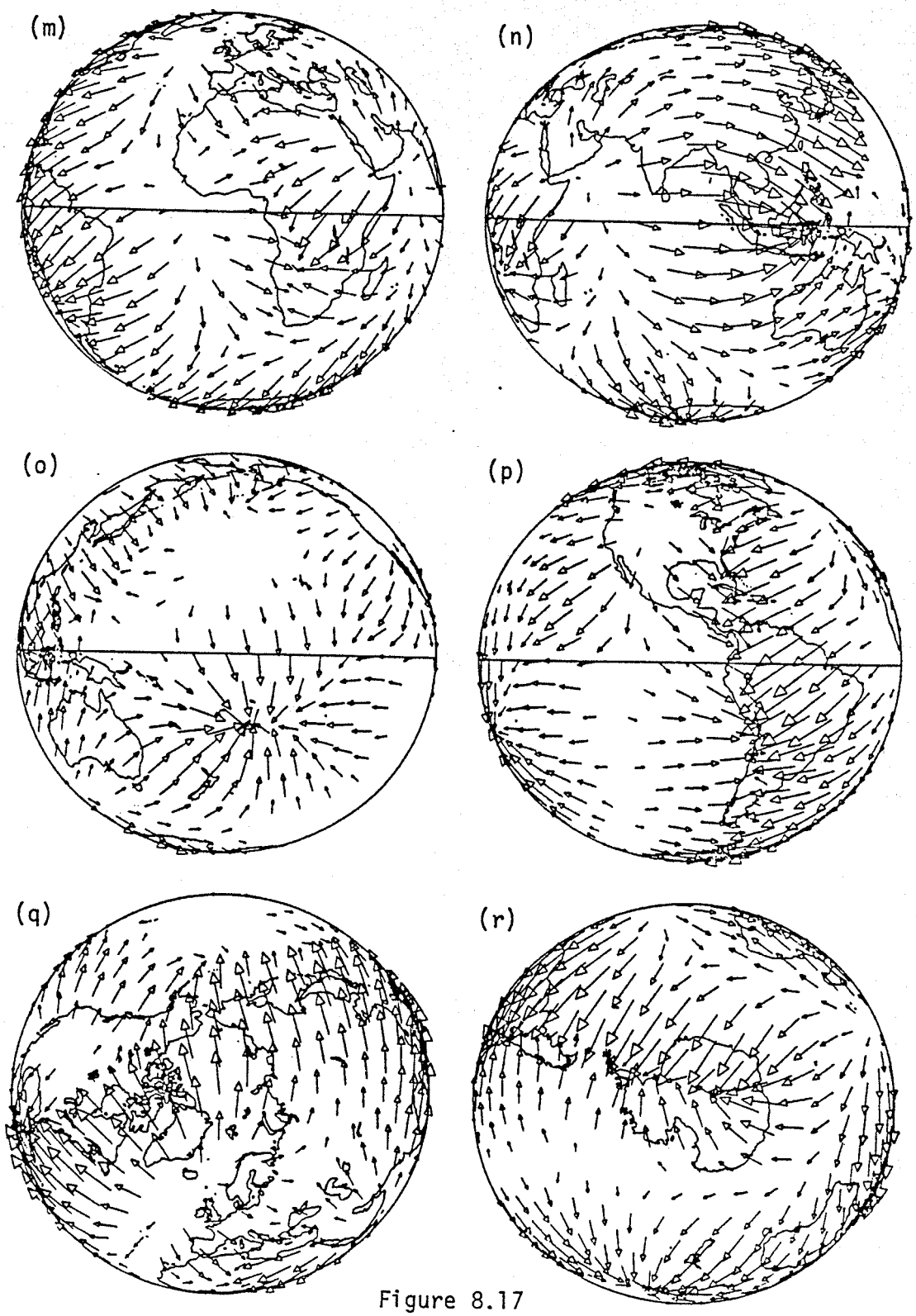

Figure 8.17

Figure 8.18. Same solution as Figure 8.17 except at approximately 0.7 overturn time. Maximum velocity for views (a)-(f) is 12.7 mm/yr, for views (g)-(l) 17.1 mm/yr, and for views (m)-(r) 13.1 mm/yr.

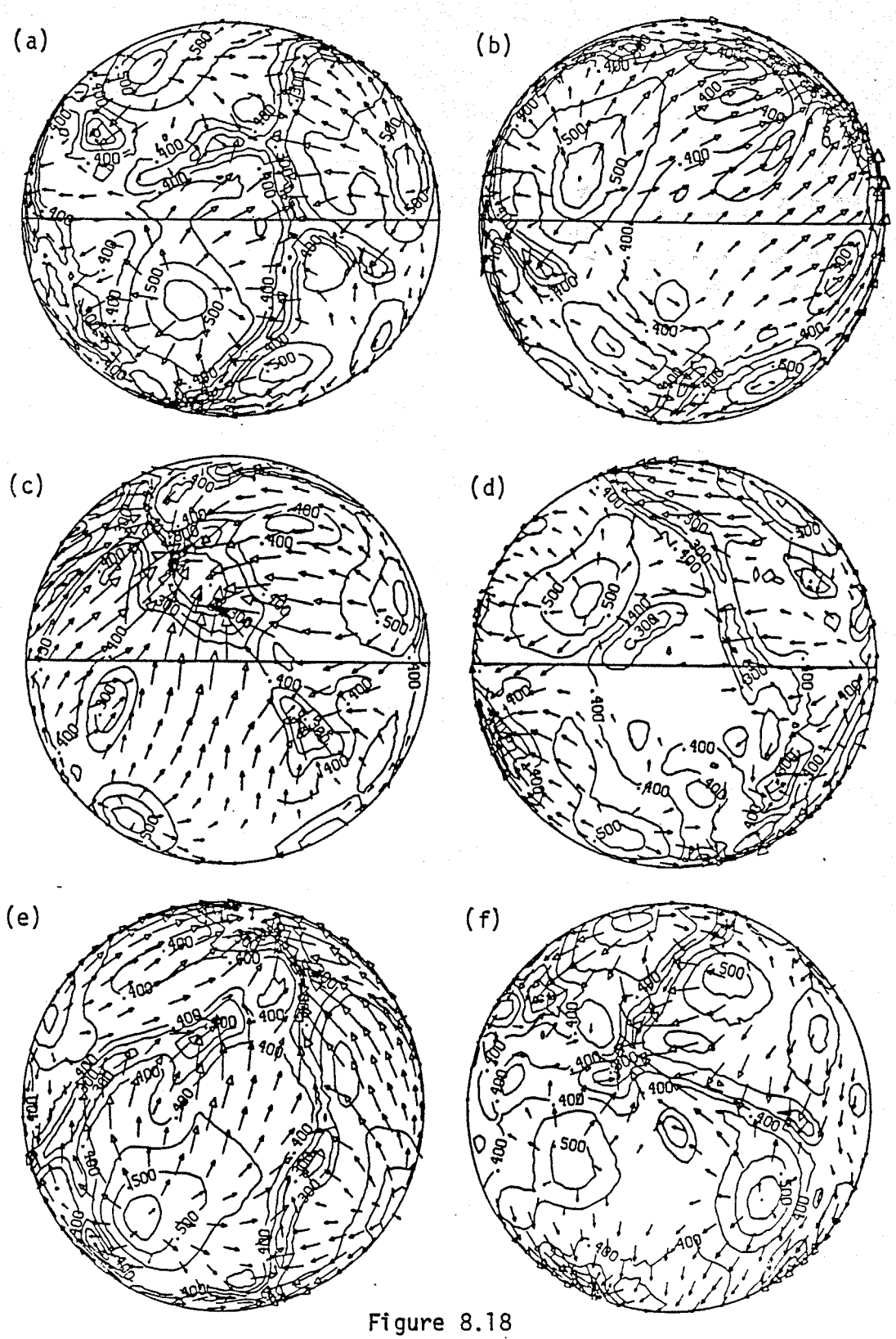

Figure 8.18

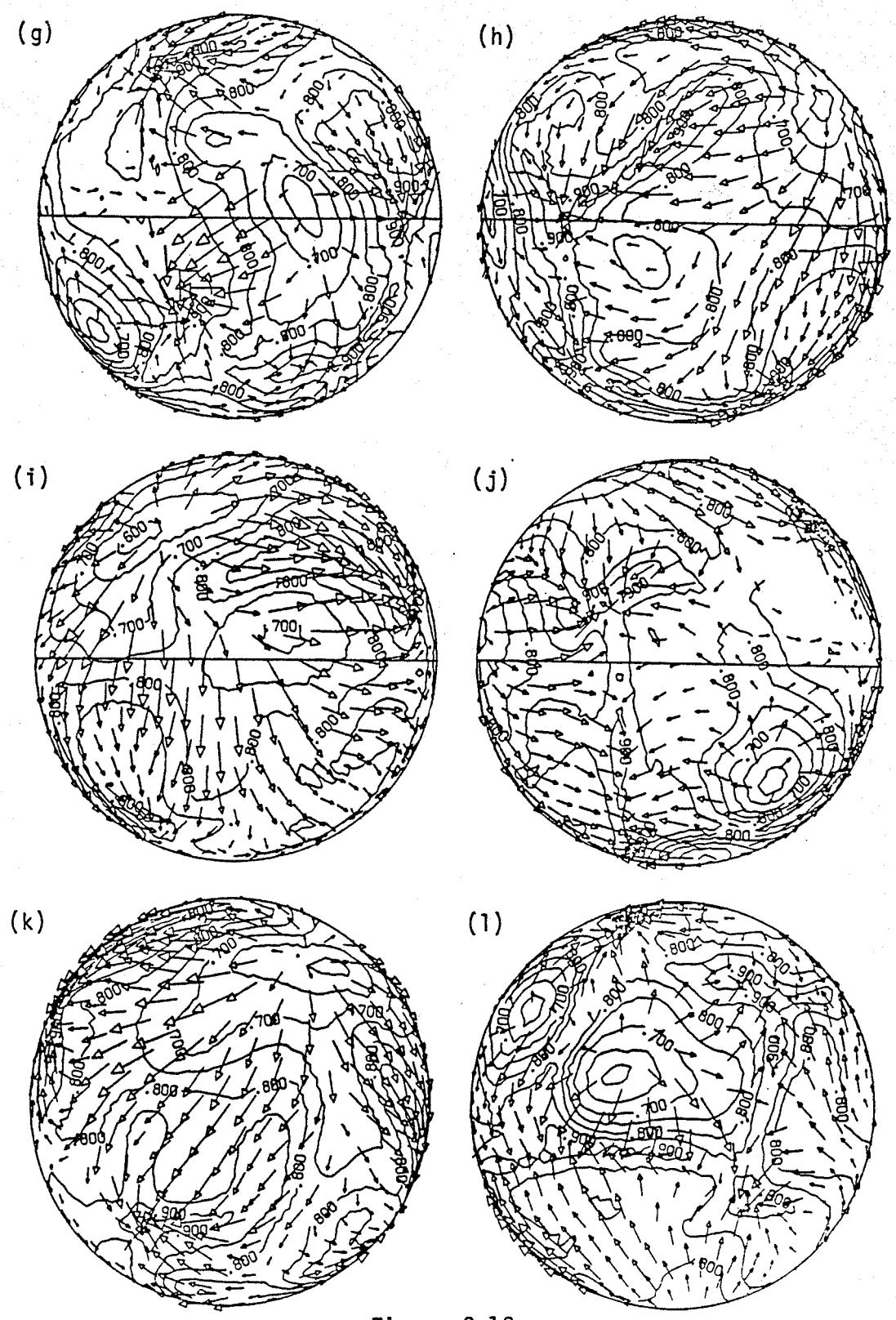

Figure 8.18

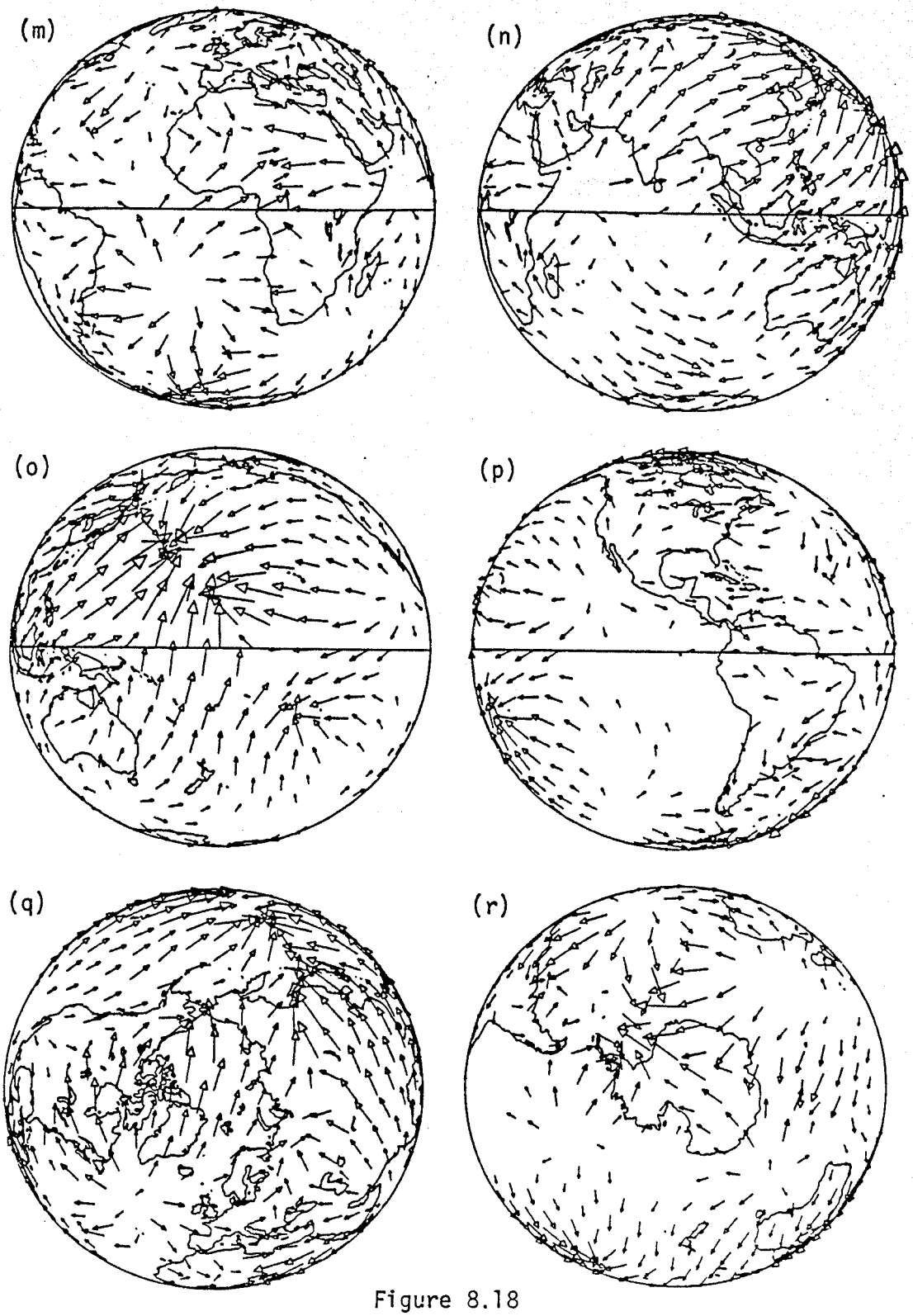

Figure 8.18

Figure 8.19. Same solution as Figure 8.17 except at approximately 1.0 overturn time. Maximum velocity for views (a)-(f) is 10.9 mm/yr and for views (g)-(l) is 20.0 mm/yr.

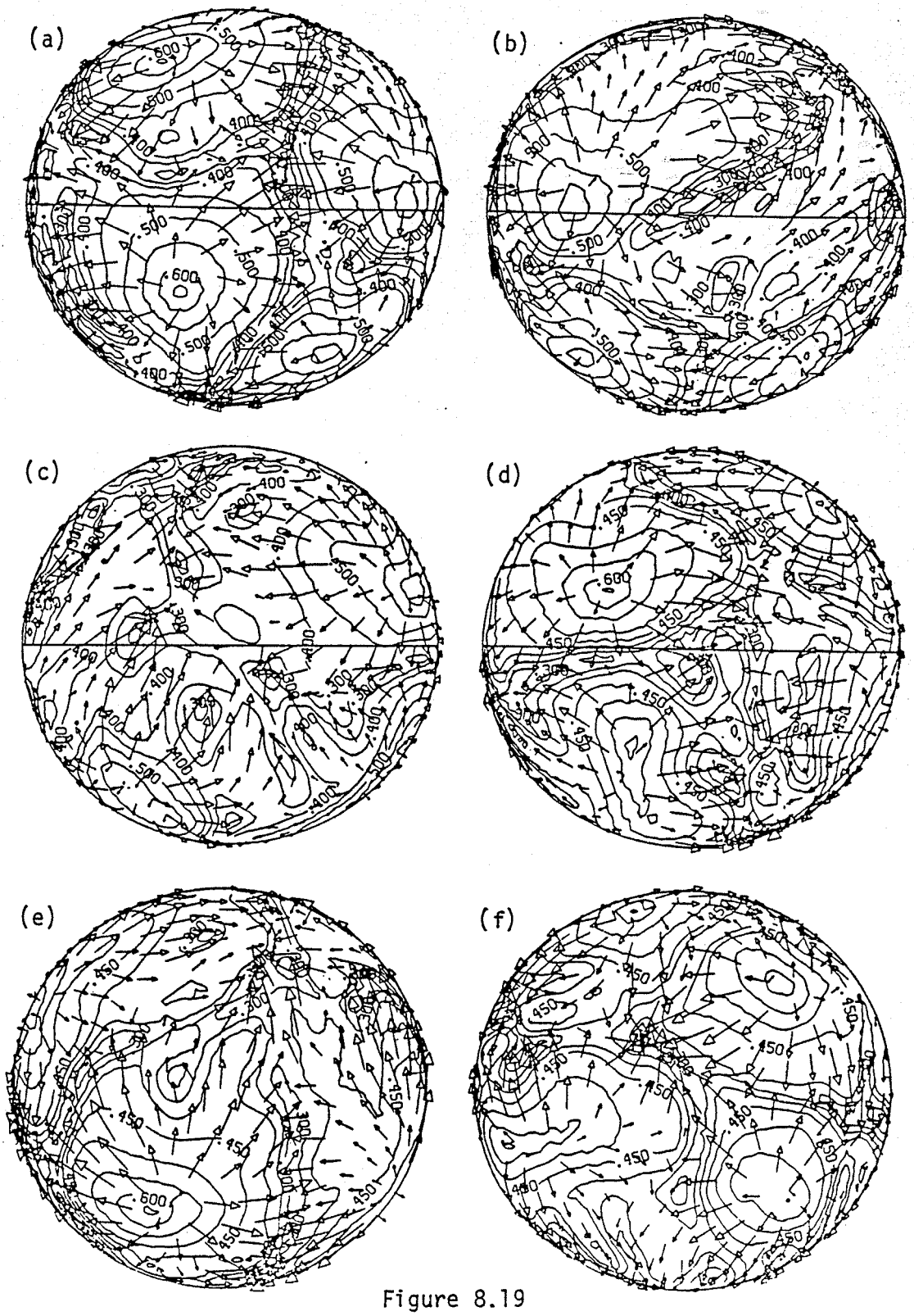

Figure 8.19

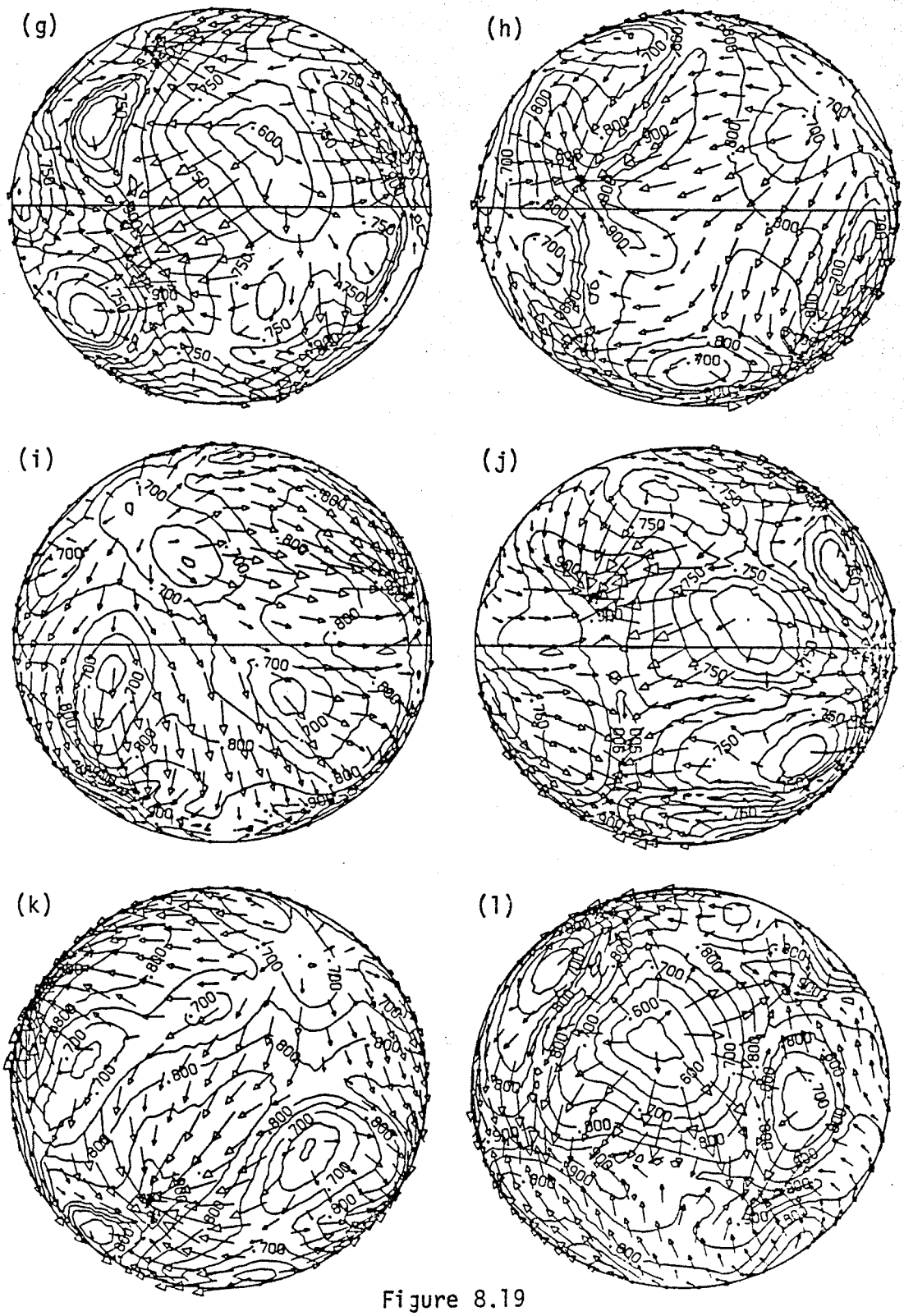

Figure 8.19

Figure 8.20. Same solution as Figure 8.17 except at approximately 1.4 overturn times. Maximum velocity for views (a)-(f) is 11.1 mm/yr, for views (g)-(l) 20.4 mm/yr, and for views (m)-(r) 11.3 mm/yr.

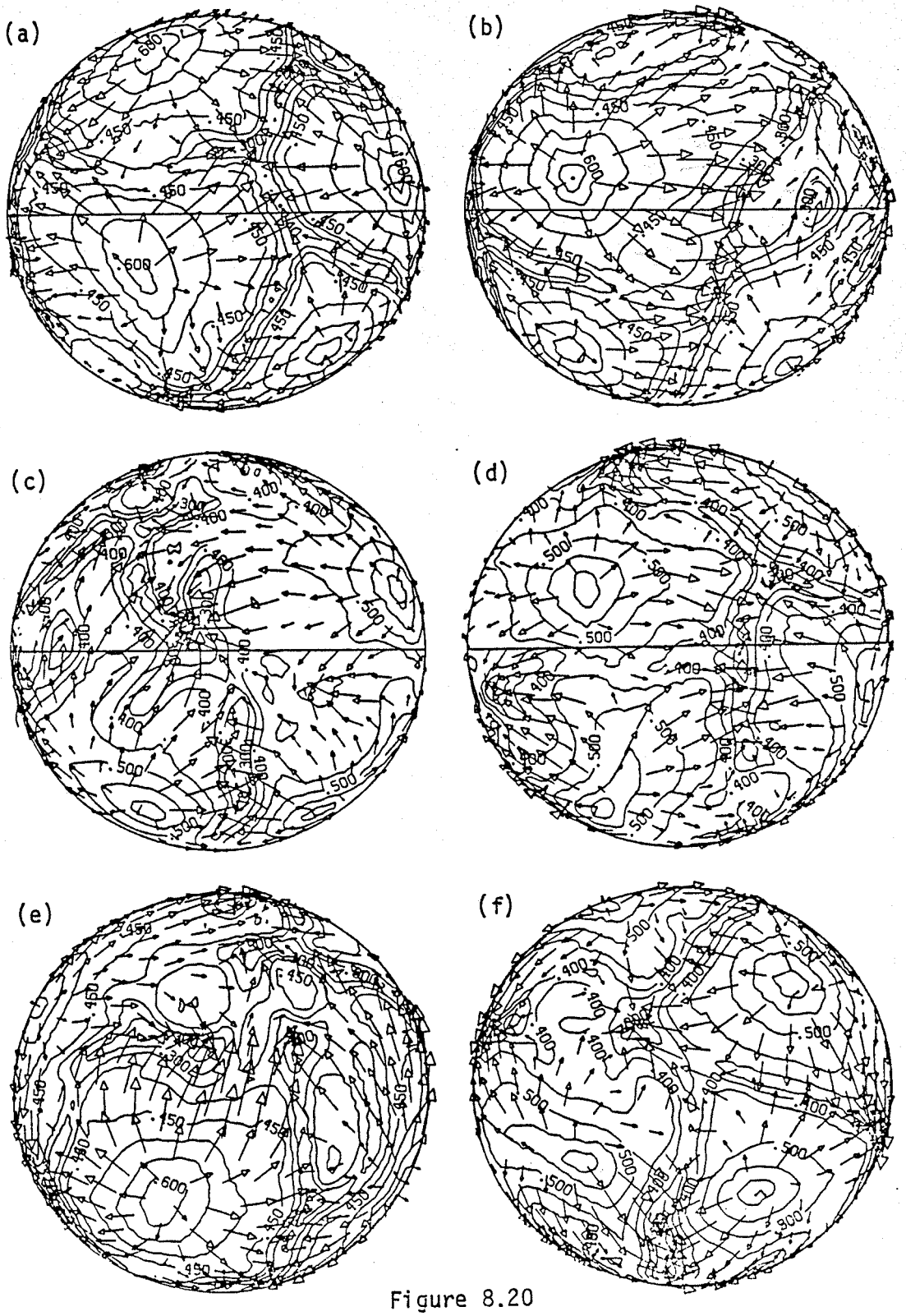

Figure 8.20

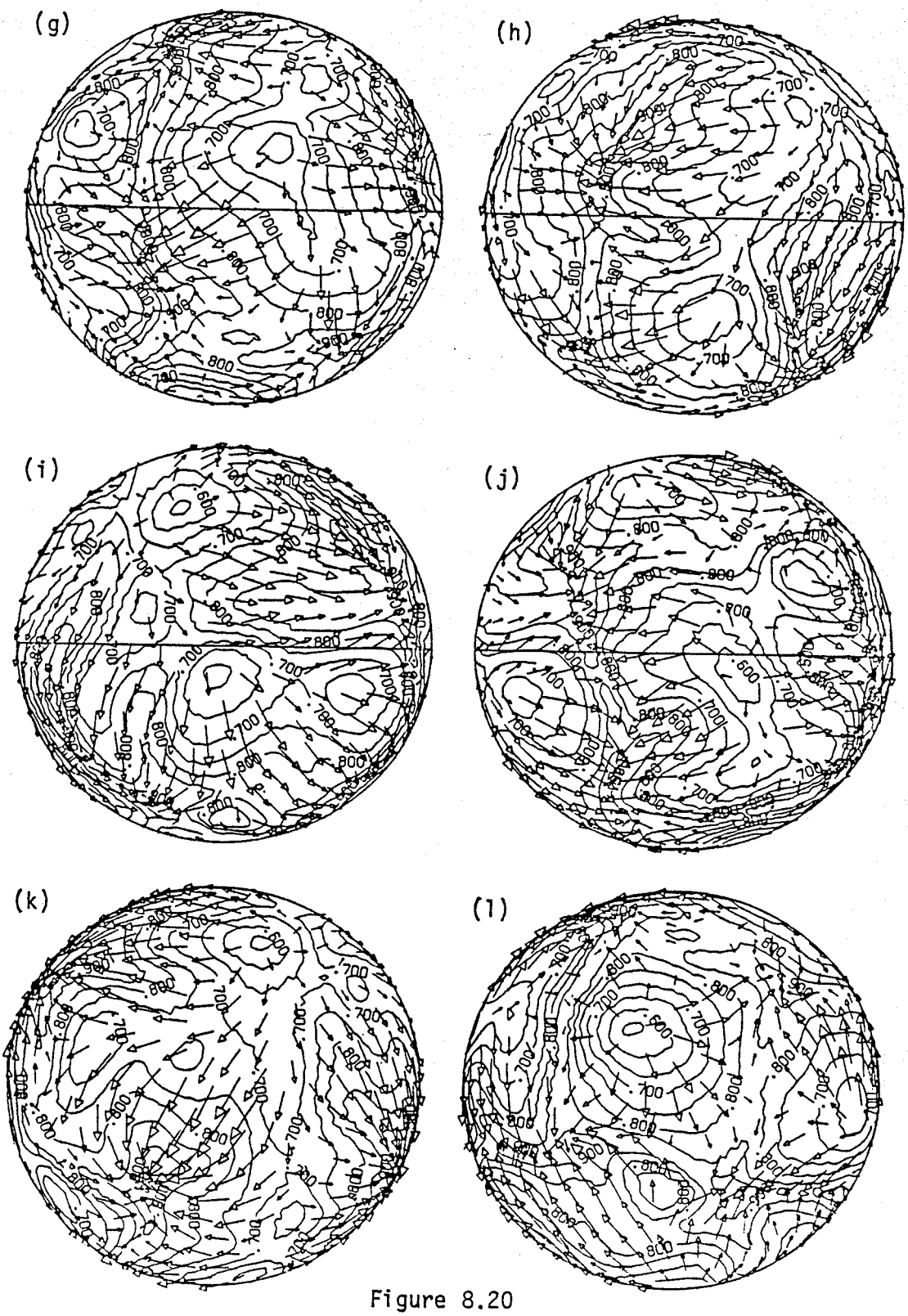

Figure 8.20

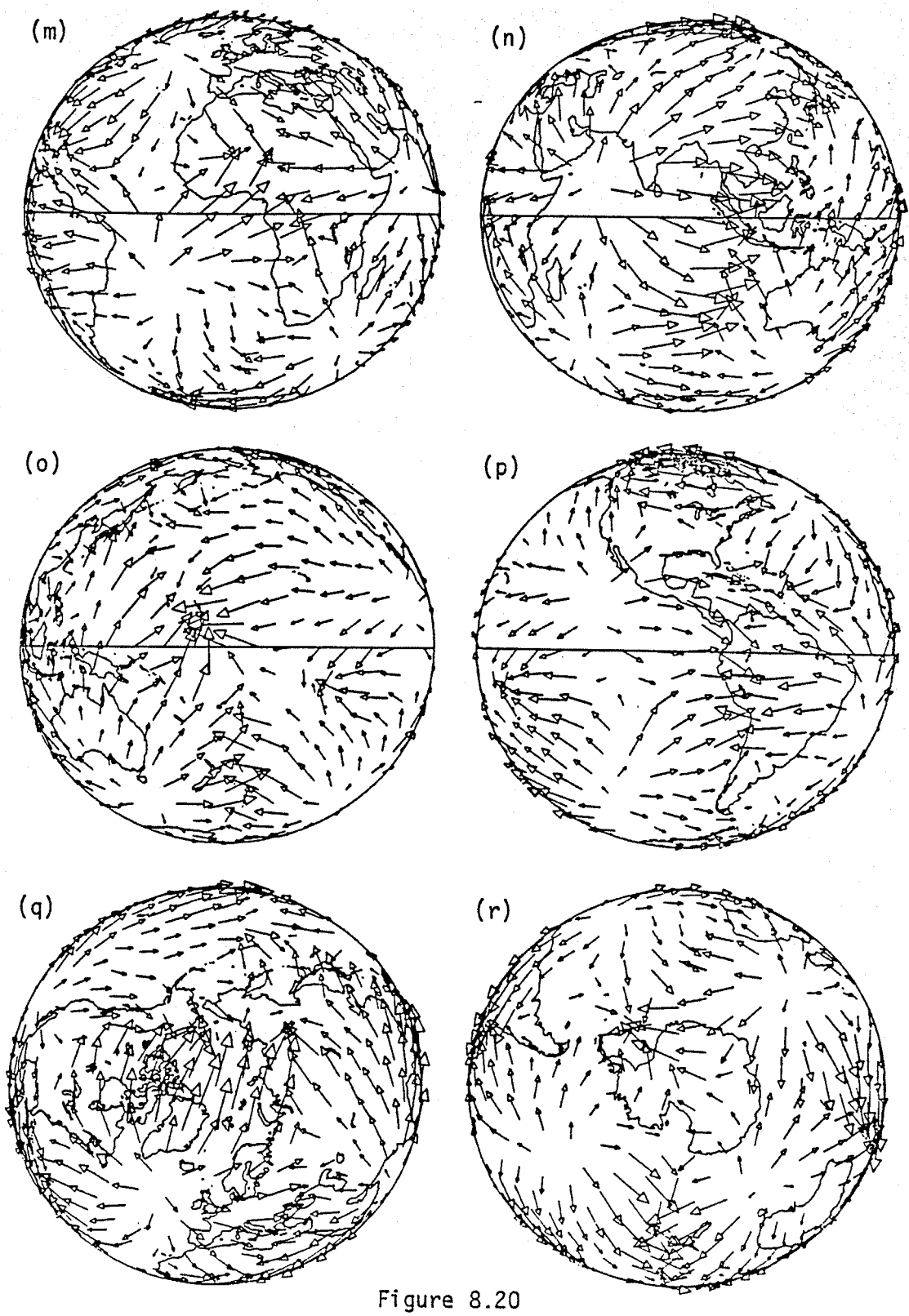

Figure 8.20

Figure 8.21. Same solution as Figure 8.17 except at approximately 1.7 overturn times. Views (a)-(f), (m)-(r), and (s)-(x) correspond, respectively, to views (a)-(f), (g)-(l), and (m)-(r) of Figure 8.17 in regard to radial position. (g)-(l) have a radial position of 4850 km. Maximum velocity for views (a)-(f) is 12.2 mm/yr, for views (g)-(l) 26.2 mm/yr, for views (m)-(r) 18.8 mm/yr, and for views (s)-(x) 12.5 mm/yr. (y)-(dd) have same significance and normalization as (m)-(r) in Figure 8.1.

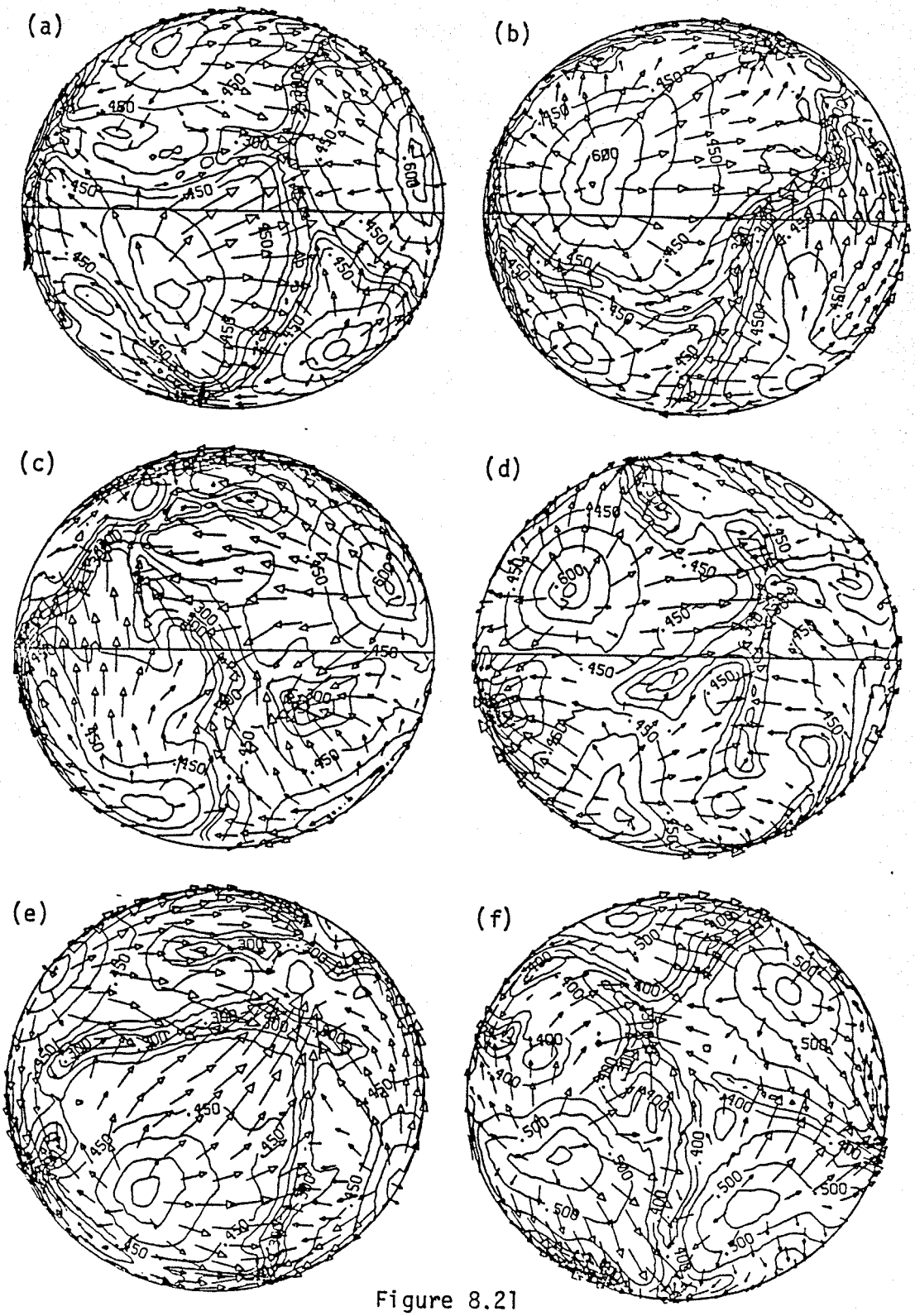

Figure 8.21

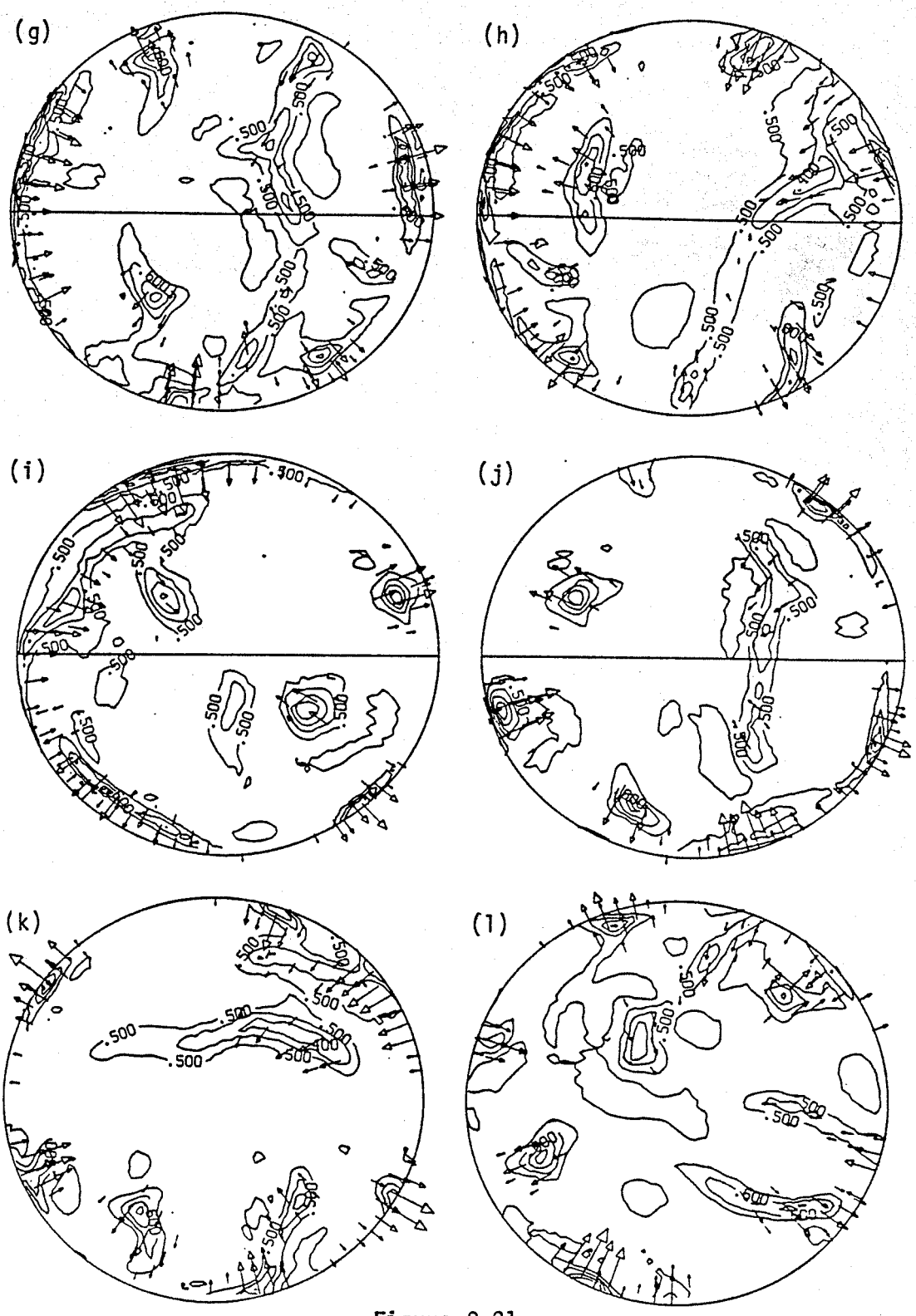

Figure 8.21

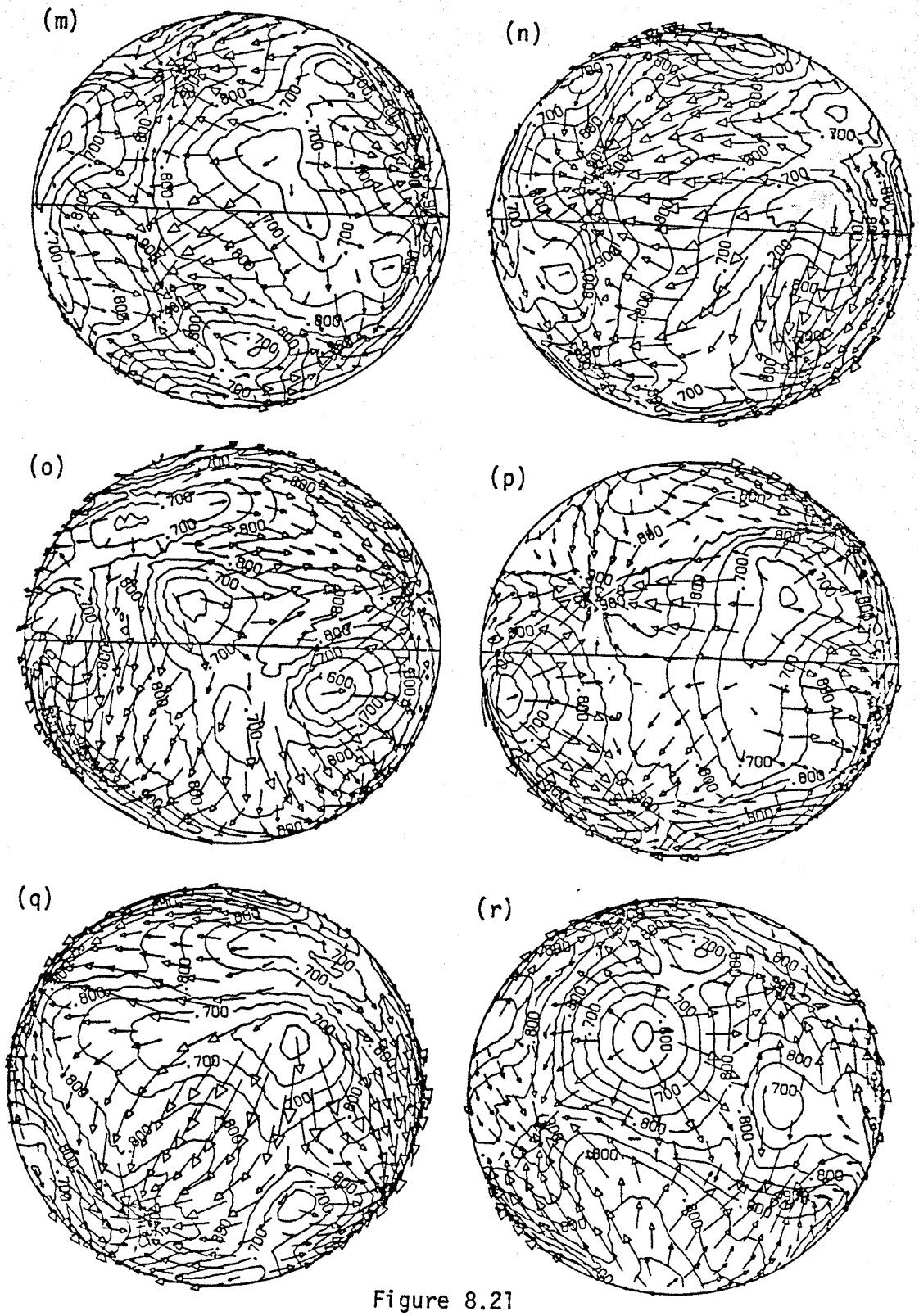

Figure 8.21

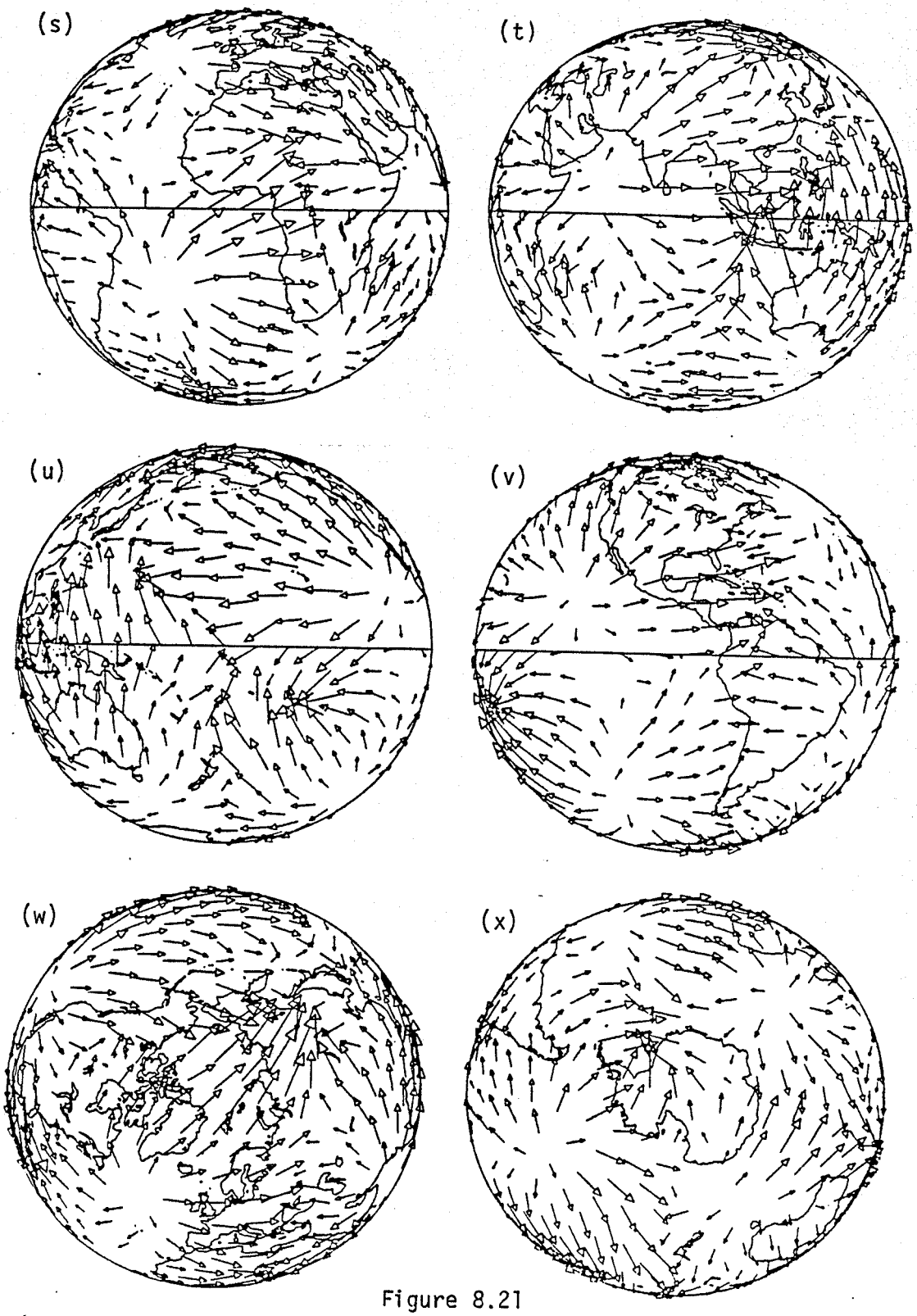

Figure 8.21

(y)

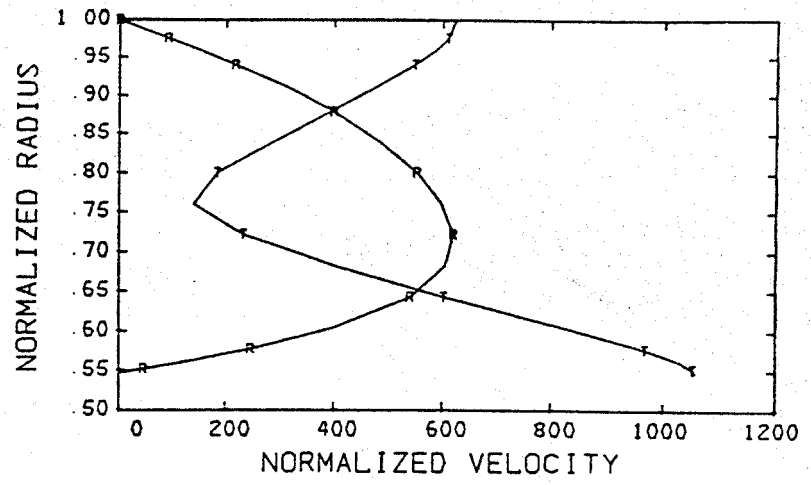

(z)

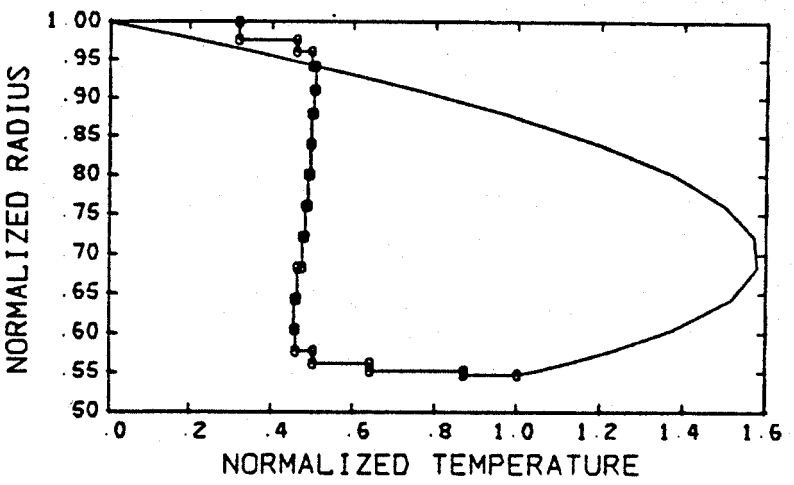

(aa)

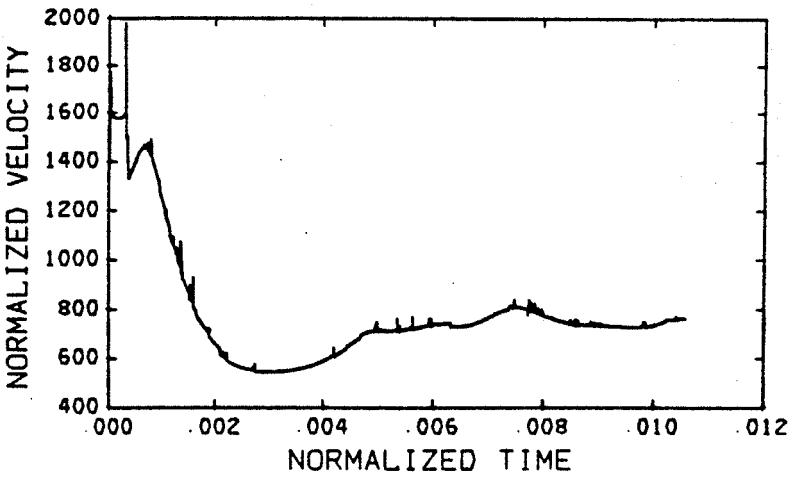

Figure 8.21

(bb)

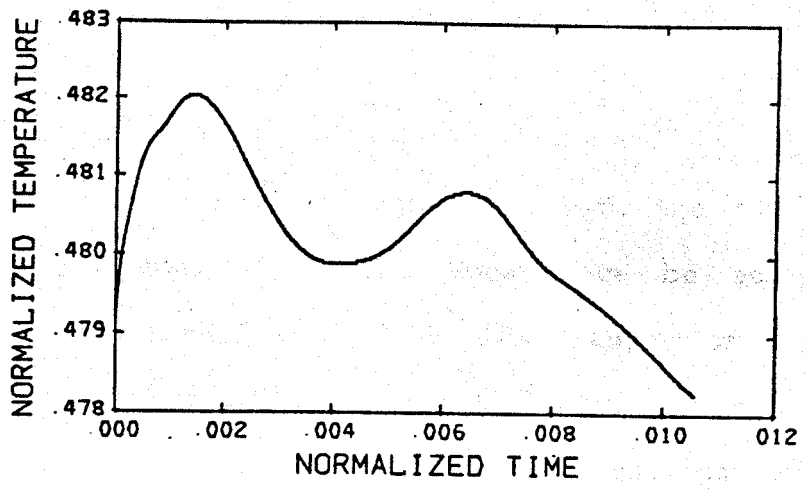

(cc)

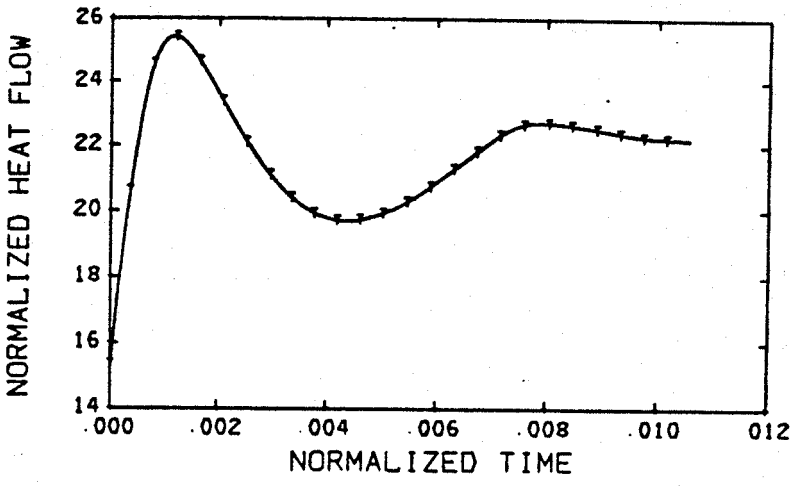

(dd)

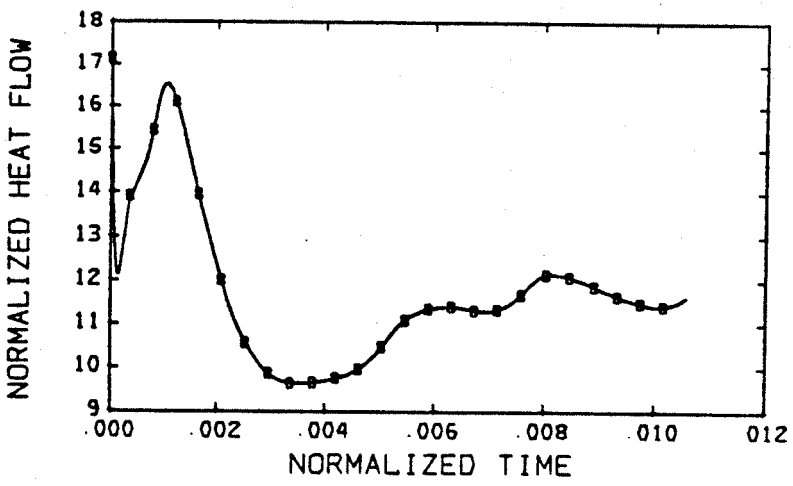

Figure 8.21

9. CONCLUSIONS

This dissertation illustrates the effectiveness of a multigrid solution technique when used in conjunction with the finite-element method and demonstrates that O(n) speed can be achieved for three-dimensional problems, where n is the number of degrees of freedom. The O(n) speed implies a savings in computational cost over other methods currently in use comparable to the savings afforded by the fast Fourier transform in spectral calculations.

The application of the multigrid technique to a spherical shell brings into focus many of the benefits derived from a discretization based on the regular icosahedron. In addition to providing a convenient means for generating a set of nested grids needed by the multigrid approximate inverse algorithm, the regular icosahedral mesh gives an almost uniform discretization of the sphere, has symmetries which can be exploited to reduce significantly operator storage and assembly costs, and produces a data structure that can be readily vectorized and partitioned for efficient implementation on a computer with multiple processors. A new finite element for the sphere based on spherical barycentric coordinates is described.

Formulation of the thermal convection problem using this numerical approach accomodates features such as compressibility and spatially varying material properties which other techniques commonly exclude. The dissertation, while limiting its scope to the case of spatially uniform properties and almost incompressible flow, nevertheless demonstrates that non-Boussinesq effects of finite bulk modulus and

finite thermal expansivity can be on the order of several percent for problems of practical interest.

Several new results are obtained for the problem of infinite Prandtl number, almost incompressible convection in a non-rotating spherical shell of radius ratio 0.5 with undeformable, free-slip boundaries, gravitational acceleration increasing linearly with radius, Newtonian rheology, and spatially uniform material properties. When heating is strictly from below, the Nusselt number is found to scale with Rayleigh number to the 0.286 power. Furthermore, the preferred pattern, for Rayleigh numbers from just above critical to at least 10^5, consists of three cells, two of which are slightly larger than the third and mirror images of each other, with upwelling at the cell centers. The pattern resembles the L = 3, M = 3 sectorial pattern with one cell smaller than the other two.

When heating is strictly from within, a similar pattern, except that downwelling occurs at the cell centers, is reached from random initial conditions for Rayleigh numbers up to 15 times critical. At still higher Rayleigh numbers the number of cells begins to increase and the downwelling becomes intense and localized in narrow columns.

When heating is partly from below and up to at least 75% from within, the mean convective velocities remain almost unchanged from the heated strictly from below case. As more internal heat is added, the interior temperature rises, the pattern modifies its form somewhat, but the heat flow through the inner boundary is only weakly reduced.

Experiments applied to the earth's mantle use a radius ratio of 0.547 and constant gravity, but otherwise involve the same

assumptions as above. Cases initialized with a temperature distribution warmer beneath present-day mid-ocean ridges and cooler adjacent to present trenches yield solutions which display surface velocities that correlate well in direction and relative magnitude with present surface velocities on the earth for times corresponding to multiple convective overturns and Rayleigh numbers from 25,000 to 10^6. At $R = 10^6$, the solution has plume-like character with the upwelling flow localized to seven plumes. Centers of three plumes are near regions of current major active mid-ocean volcanic activity. Power-law scaling of these results to a Rayleigh number of 2×10^7, appropriate to whole-mantle convection, yields an RMS surface velocity of 37 mm/yr. Since this number is close to the observed value, these results appear to favor whole-mantle convection instead of two-layer convection, as the latter has significantly lower convective efficiency.

REFERENCES

Anderson, O.L. and J.R. Baumgardner, Equations of state in planet interiors, Proc. Lunar Planet. Sci. Conf. 11th, 1999-2014, 1980.

Baumgardner, J.R., and P.O. Frederickson, Icosahedral discretization of the two-sphere. (to appear)

Benson, M.W., and P.O. Frederickson, Iterative solution of large sparse linear systems arising in certain multidimensional problems, Util. Math, 22, 127-140, 1982.

Bird, P. and J. Baumgardner, Fault friction, regional stress, and crust-mantle coupling in southern California from finite-element models, J. Geophys. Res., (submitted), 1983.

Boss, A.P., Convection, Rev. Geophys. Space Phys., 21, 1511-1520, 1983.

Busse, F.H., Patterns of convection in spherical shells, J. Fluid Mech., 72, 67-85, 1975.

Busse, F.H., Non-linear properties of thermal convection, Rep. Prog. Phys., 41, 1929-1967, 1978.

Busse, F.H., and N. Riahi, Patterns of convection in spherical shells. Part 2, J. Fluid Mech., 123, 283-301, 1982.

Chandrasekhar, S., Hydrodynamic and Hydromagnetic Stability, Clarendon Press, Oxford, 1961.

Christensen, U., Convection in a variable viscosity fluid: Newtonian versus power-law rheology, (unpublished manuscript).

Cullen, M.J.P., Integrations of the primitive equations on a sphere using the finite element method. Quart. J. R. Met. Soc., 100, 555-562, 1974.

Frederickson, P.O., Fast approximate pseudo inversion of large sparse linear systems (to appear).

Galerkin, B.G., Series solution of some problems of elastic equilibrium of rods and plates (Russian), Vestn. Inzh. Tech., 19, 897-908, 1915.

Herring, C., Diffusional viscosity of a polycrystalline solid, J. Appl. Phys., 21, 437-450, 1950.

Riahi, N., G. Geiger, and F.H. Busse, Finite Prandtl number convection in spherical shells, Geophys. Astrophys. Fluid Dyn., 20, 307-318, 1982.

Sadourny, R., A. Arakawa, and Y. Mintz, Integration of the nondivergent barotropic vorticity equation with an icosahedral-hexagonal grid for the sphere, Month. Weather Rev., 96, 351-356, 1968.

Schubert, G., Subsidus convection in the mantles of terrestrial planets, Ann. Rev. Earth Planet. Sci., 7, 289-342, 1979.

Schubert, G., and A. Zebib, Thermal convection of an internally heated infinite Prandtl number fluid in a spherical shell, Geophys. Astrophys. Fluid Dyn., 15, 65-90, 1980.

Stacey, F.D., B.J. Brennan, and R.D. Irvine, Finite strain theories and comparisons with seismological data, Geophys. Surveys, 4, 189-232, 1981.

Torrance, K.E., Numerical approaches to solid-state convection in planetary bodies, Phys. Earth Planet. Int., 19, 158-167, 1979.

Turcotte, D.L., A.T. Hsui, K.E. Torrence, and G. Schubert, Influence of viscous dissipation on Benard convection, J. Fluid Mech., 64, part 2, 369-374, 1974.

Vestine, E.H., W.L. Sibley, J.W. Kern, and J.L. Carlstedt, Integral and spherical-harmonic analyses of the geomagnetic field for 1955.0, part 2, J. Geomag. Geoelectr., 15, 73-89, 1963.

Weertman, J., and J.R. Weertman, High temperature creep of rock and mantle viscosity, Ann. Rev. Earth Planet. Sci., 3, 293-315, 1975.

Williamson, D.L., Integration of the barotropic vorticity equation on a spherical geodesic grid, Tellus, 20, 642-653, 1968.

Young, R.E., Finite-amplitude thermal convection in a spherical shell, J. Fluid Mech., 63(4), 695-721, 1974.

Zebib, A., G. Schubert, and J. M. Straus, Infinite Prandtl number thermal convection in a spherical shell, J. Fluid Mech., 97(2), 257-277, 1980.

Zebib, A., G. Schubert, J.L. Dein, and R.C. Paliwal, Character and stability of axisymmetric thermal convection in spheres and spherical shells, Geophys. Astrophys. Fluid Dyn., 23, 1-42, 1983.

Zienkiewicz, O.C., The Finite Element Method, (3rd ed.), McGraw-Hill, London, 787 pp., 1977.